The Astronomical Journal, 166:236 (18pp), 2023 December https://doi.org/10.3847/1538-3881/acfaa1

Empirical 2MASS–WFC3/IR Filter Transformations Across the H-R Diagram from Synthetic Photometry

M. J. Durbin[1,2], R. L. Beaton[3,4,5,6], A. J. Monson[7,8], B. Swidler[5], and J. J. Dalcanton[2,9]
[1] Department of Astronomy, University of California, Berkeley, Berkeley, CA 94720, USA; meredith.durbin@berkeley.edu
[2] Department of Astronomy, University of Washington, Box 351580, U.W., Seattle, WA 98195-1580, USA
[3] Space Telescope Science Institute, Baltimore, MD 21218, USA
[4] Department of Physics and Astronomy, Johns Hopkins University, Baltimore, MD 21218, USA
[5] Department of Astrophysical Sciences, Princeton University, 4 Ivy Lane, Princeton, NJ 08544, USA
[6] The Observatories of the Carnegie Institution for Science, 813 Santa Barbara Street, Pasadena, CA 91101, USA
[7] Department of Astronomy & Astrophysics, The Pennsylvania State University, 525 Davey Lab, University Park, PA 16802, USA
[8] Department of Astronomy/Steward Observatory, University of Arizona, 933 North Cherry Avenue, Tucson, AZ 85721, USA
[9] Center for Computational Astrophysics, Flatiron Institute, 162 Fifth Avenue, New York, NY 10010, USA
Received 2023 August 11; revised 2023 September 8; accepted 2023 September 9; published 2023 November 9

Abstract

Near-infrared bandpasses on spaceborne observatories diverge from their ground-based counterparts as they are free of atmospheric telluric absorption. Available transformations between respective filter systems in the literature rely on theoretical stellar atmospheres, which are known to have difficulties reproducing the observed spectral energy distributions of cool giants. We present new transformations between the Two Micron All Sky Survey JHK_S and Hubble Space Telescope WFC3/IR F110W, F125W, and F160W photometric systems based on synthetic photometry of empirical stellar spectra from four spectral libraries. This sample comprises over 1000 individual stars, which together span nearly the full H-R diagram and sample stellar populations from the solar neighborhood out to the Magellanic Clouds, covering a broad range of ages, metallicities, and other relevant stellar properties. In addition to global color-dependent transformations, we examine band-to-band differences for cool, luminous giant stars in particular, including multiple types of primary distance indicators.

Unified Astronomy Thesaurus concepts: Calibration (2179); Infrared astronomy (786); Photometric systems (1233); Stellar colors (1590); Stellar populations (1622)

Supporting material: machine-readable tables

1. Introduction

Near-infrared (NIR) spectrophotometry of stars is increasingly important to a wide range of astrophysical issues. Recent and upcoming missions with NIR capabilities, such as JWST and Roman, will resolve orders of magnitude more stars at higher precision and greater distances than their closest predecessors.

In practice, however, the potential of these and other space-based observations is frequently limited by the ability to link new photometry to the rich legacy of ground-based observations (e.g. the Two Micron All Sky Survey (2MASS); Skrutskie et al. 2006). The widely used *JHK* filter set and its near relatives are largely shaped to accommodate the atmospheric windows where the Earth's atmosphere is transparent. Space-based instruments, however, do not share these constraints, and can sample the full range of the stellar spectrum. Even for space-based filters expressly designed to mimic their ground-based counterparts, subtle differences can arise from the atmospheric absorption that typically defines ground filters' blue and red edges. Similarly, spatial and temporal variations in Earth's atmosphere add complexity to the task of consistently calibrating ground-based NIR photometry, both night to night and across observatories.

Interpreting even precisely calibrated NIR photometry is particularly challenging for the cool and luminous giants that dominate the integrated rest-frame infrared light of intermediate-aged to ancient stellar populations. In such stars, low surface gravities ($\log g \lesssim 1$) and effective temperatures ($T_{\rm eff} \lesssim 4000$ K) give rise to deep and wide atomic and molecular absorption features that can have profound impacts on spectral shapes as measured with typical broadband filters. Figure 1 shows example spectral sequences for three broad subclasses of such stars: nonpulsating asymptotic giant branch (AGB) or bright first-ascent red giant branch (RGB) stars ("quasi-static" giants, following Verro et al. 2022a), and thermally pulsing AGB (TP-AGB) stars with carbon- and oxygen-rich atmospheres. We overlay synthetic integrated flux densities for each spectrum in the ground-based 2MASS JHK_S and Hubble Space Telescope Wide Field Camera 3 (HST/WFC3) F110W and F160W filters. While the integrated flux densities in overlapping HST and 2MASS bandpasses approximately agree for the quasi-static giants, they begin to diverge as molecular feature strength increases in both TP-AGB subtypes. Furthermore, even nonpulsating giants exhibit variability over a range of amplitudes, timescales, and modes due to asteroseismic oscillations, further complicating their photometric calibration.

In this paper, we begin a systemic empirical cross-calibration of the ground-based 2MASS filter set with a subset of popular broadband filters on the infrared channel of HST's WFC3. We take advantage of several empirical spectral libraries that have been released in the past two decades, which together include

Table 1
Summary of Spectral library Data Sets Used in This Work

	(E)IRTF	XSL DR3	CALSPEC			All
Facility	IRTF/SPEX	VLT/X-shooter	STIS	NICMOS	WFC3/IR	⋯
Wavelength range [μm]	0.8–2.5+	0.3–2.45	0.1–1.0	0.8–2.5	0.8–1.7	⋯
Spectral resolution	∼2000	∼10,000	>500	∼200	∼170	⋯
Absolute fluxing?	Yes, to 2MASS	No		Yes		⋯
Primary reference(s)	Rayner et al. (2009) Villaume et al. (2017)	Verro et al. (2022b)		Turnshek et al. (1990) Bohlin et al. (2014)		⋯
Spectral types	Primarily late-type	Many		Primarily dwarfs		⋯
Total spectra	431	736		102		1269
Unique stars	422	614		102		1061
$J - K_S$ color range	−0.1–2.5	−0.2–2.4		−0.3–0.9		−0.3–2.5

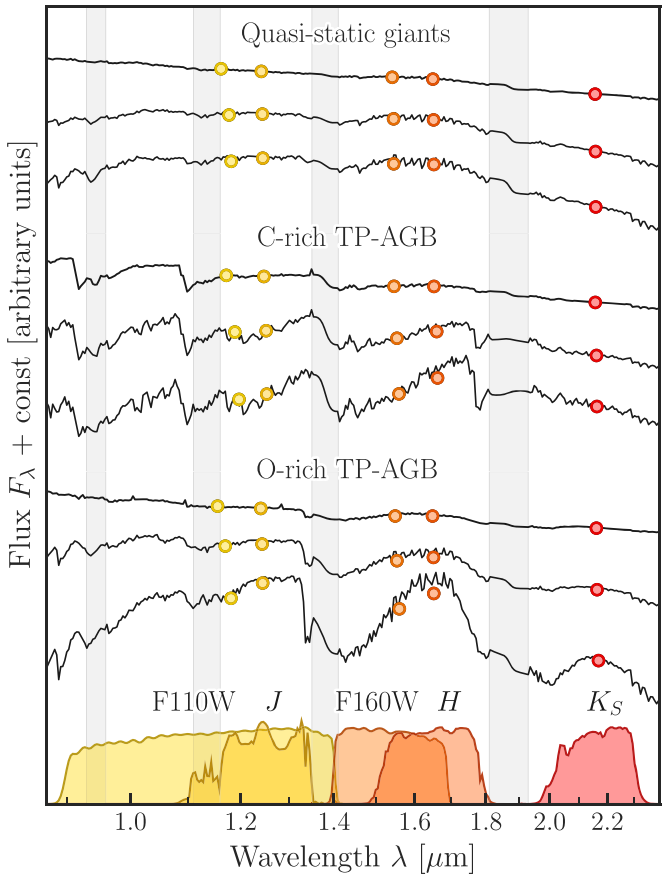

Figure 1. Schematic comparison of NIR stellar spectra (black lines; Verro et al. 2022a) and their integrated flux densities (colored points, plotted at respective effective wavelengths) for three broad classes of cool and luminous giants. These include nonpulsating AGB and upper RGB stars (upper three), and TP carbon-rich (center) and oxygen-rich (lower) AGB stars, respectively. Transmission curves for the 2MASS JHK_S and HST F110W and F160W bandpasses are shown as filled curves at the bottom, and regions with significant atmospheric telluric absorption are marked by gray vertical bands.

stars ranging in temperature from below 3000 K to over 60,000 K. At the higher temperatures, the sample is dominated by main-sequence stars and white dwarfs, and at cool temperatures, the sample is approximately evenly split between low-mass dwarfs and evolved giants.

Section 2 describes the data products used in this work, including all spectral libraries, distance and extinction estimates, and other literature data used in determining and interpreting our final synthetic magnitudes and colors. Section 3 describes our synthetic photometry production and validation process. In Section 4 we present best-fit global 2MASS ↔ HST/WFC3-IR magnitude and color transformations. We compare to previously published relations and examine residuals with respect to stellar properties in Section 5, and discuss conclusions and future work in Section 6.

2. Data

In this section, we describe the data sets used in this work: empirical spectral libraries (Section 2.1); distance and reddening measurements (Section 2.2); and other compiled literature parameters (Section 2.3).

2.1. Empirical Spectral Libraries with NIR Coverage

Empirical spectral libraries are critical benchmarks for understanding many facets of stellar atmospheres, evolution, and populations (Trager 2012). Many existing libraries offer excellent coverage of optical and near-ultraviolet wavelengths (e.g. Prugniel & Soubiran 2001, 2004; Bagnulo et al. 2003; Le Borgne et al. 2003; Valdes et al. 2004; Gregg et al. 2006; Sánchez-Blázquez et al. 2006; Prugniel et al. 2007; Falcón-Barroso et al. 2011; Wang et al. 2018; Yan et al. 2019). However, there is a relative dearth of comparable libraries available for the NIR. Such observational libraries are essential, given that theoretical spectra are known to have difficulty reproducing the observed NIR spectral energy distributions (SEDs) and spectral features of cool and luminous giants (Alvarez et al. 2000; Tej et al. 2003; Bonatto et al. 2004; Maraston 2005; Levesque et al. 2006; Lyubenova et al. 2012; Aringer et al. 2016, 2019; Gonneau et al. 2017; Baldwin et al. 2018; Dahmer-Hahn et al. 2018; Coelho et al. 2020; Lancon et al. 2021; Eftekhari et al. 2022; Eriksson et al. 2023).

The spectral library data sets adopted in this work were selected to have continuous spectral coverage in the range of at least $0.8 \lesssim \lambda \lesssim 1.8$ μm, with the SED continuum preserved. In addition to the descriptions that follow, basic characteristics of the libraries and the stars adopted from them are provided in Table 1. For all of the stars selected from the libraries, we also search the literature and archives such as SIMBAD for relevant optical and infrared photometry, stellar parameters and classifications, distances, and line-of-sight extinctions. Because this information is extensive and potentially of use for other purposes, we include machine-readable tables of our final compiled database in Appendix A.

2.1.1. CALSPEC

CALSPEC is a library of spectrophotometric standards that forms the basis of the HST absolute flux calibration scale[10] (Turnshek et al. 1990; Bohlin et al. 2001; Bohlin 2007; Bohlin & Cohen 2008; Bohlin et al. 2014; Bohlin & Deustua 2019, and references therein). The majority of observed spectra are taken with the Space Telescope Imaging Spectrograph (STIS), WFC3/IR, and/or the Near Infrared Camera and Multi-Object Spectrometer (NICMOS) instruments. STIS covers 0.011–1.03 μm at low to medium resolution with a number of gratings/grisms; only the G750L and G750M span into the IR, with resolutions of ∼500–1000 and ∼5000–9000, respectively over, ∼0.5–1. μm. The WFC3/IR grisms G102 and G140 together span 0.8–1.7 μm, at resolutions of $R = 210$ at 1 μm and 130 at 1.4 μm. The NICMOS grisms span from 0.8 to 2.5 μm with resolution $R \sim 200$. Most CALSPEC stars have counterpart theoretical spectra available as well (Bohlin et al. 2017), and regions of the empirical spectra that lack observational coverage are filled in with model predictions where available. We do not retain stars without empirical WFC3/IR and/or NICMOS data in our final analysis, but show them in Section 3.2 for comparison.

In addition to CALSPEC's subpercent absolute and relative calibration and widespread use as standards (e.g. Holberg & Bergeron 2006; Casagrande et al. 2010; Bessell & Murphy 2012; Tonry et al. 2012; Scolnic et al. 2018), its lack of atmospheric absorption makes it an extraordinarily valuable anchor, as the other spectral libraries we use are all from ground-based observatories.

Throughout this work, we use the 2023 February CALSPEC release, which includes the Vega spectrum `alpha_lyr_stis_011.fits`. We use this spectrum as our reference for the Vega magnitude system in all bands.

2.1.2. IRTF and EIRTF Libraries

The original Infrared Telescope Facility (IRTF) Spectral Library[11] (Rayner et al. 2009) contains 226 $R \sim 2000$ spectra of 225 late-type stars at mostly solar metallicity, taken by the SpeX prism spectrograph at the NASA IRTF on Maunakea (Rayner et al. 2003) with coverage from 0.8 to 2.5+ μm. We adopt the data as presented in the library, which relied on the data processing tool described in Cushing et al. (2004), the telluric correction described in Vacca et al. (2003), and the uncertainty propagation described in Vacca et al. (2004).

The Extended IRTF Library (EIRTF; Villaume et al. 2017)[12] expands the metallicity range of the original library, adding spectra of 206 stars with $-1.7 < [\mathrm{Fe/H}] < 0.6$ taken with the same instrument. Both phases of the IRTF libraries are flux calibrated to 2MASS photometry (see Rayner et al. 2009, their Section 2.3).

2.1.3. X-shooter Spectral Library

The X-shooter Spectral Library[13] (Chen et al. 2014; Gonneau et al. 2020; Verro et al. 2022b) was designed to bridge the optical and NIR for studies of intermediate- to old-aged stellar populations. As such, it spans a wide range of spectral types and luminosity classes with an emphasis on cool giants, including first-ascent red giants, red supergiants, and both oxygen- and carbon-rich TP-AGB stars (Gonneau et al. 2016; Lancon et al. 2018). As of the third data release (Verro et al. 2022b), the library comprises 830 spectra of 683 unique stars observed with the ultraviolet, visible, and NIR arms of the Very Large Telescope (VLT)/X-shooter spectrograph simultaneously. The final set of arm-merged spectra offer $R \sim 10{,}000$ spectral coverage from 0.35 to 2.48 μm. Of these, 736 (89%; 614 unique stars) are fully corrected for wavelength-dependent instrumental flux losses (as described in Gonneau et al. 2020).

Detailed comparisons between XSL and other empirical spectral libraries, as well as between synthetic and observed Gaia and 2MASS broadband colors, find overall agreement of 5% or better for common nonvariable stars in all cases, and 1% or better in many (Gonneau et al. 2020; Verro et al. 2022b). Comparisons with model atmospheres and literature fundamental parameters, however, highlight ongoing difficulties in reproducing both the overall SED shapes and specific spectral features for stars at low temperatures ($T_{\mathrm{eff}} \lesssim 4000$ K) and surface gravities ($\log g \lesssim 1$; Gonneau et al. 2017; Arentsen et al. 2019; Lancon et al. 2021).

2.2. Distances and Reddenings

While absolute-scale synthetic fluxes are neither necessary nor practical for our purposes, line-of-sight reddenings are important for interpreting synthetic colors. All of the spectral libraries in Section 2.1 provide dereddened spectra with the exception of CALSPEC, which offers reddened model spectra instead (and whose targets are largely low-extinction regardless). However, we opt to deredden all of the spectra as uniformly as possible using independent $E(B-V)$ estimates for interlibrary consistency.

For the majority of Galactic stars, we are able to utilize three-dimensional (3D) dust maps to obtain the best estimate of reddening along the line-of-sight to the star. Thus, the process of adopting reddening has two steps: first, the determination of the distance to the star and second, the estimation of the reddening from maps.

2.2.1. Distances

For the vast majority of Galactic field stars we use geometric distances from Bailer-Jones et al. (2021). These distances use a Bayesian framework to invert the Gaia EDR3 trigonometric parallaxes and derive realistic uncertainties using a Galactic disk prior. We find available distances for 1030 stars in this catalog, but 136 of these are superseded by distances to parent objects as described below, such that only 894 stars have distances adopted directly from Bailer-Jones et al. (2021).

For stars that are members of Galactic stellar clusters, we use the mean distances derived in Cantat-Gaudin & Anders (2020) and Baumgardt & Vasiliev (2021) for open and globular clusters, respectively. Both of these works combine astrometric and kinematic information for individual stars to determine aggregate cluster distances. Cantat-Gaudin & Anders (2020) provided catalogs with membership probabilities at a star-by-star level, and we adopt the cluster distance for library stars that have cluster membership probabilities greater than 50%, which 17 stars in our sample do. For globular cluster candidate stars, we determine cluster membership by first querying SIMBAD for hierarchical parent membership probabilities. For stars with

[10] https://archive.stsci.edu/hlsps/reference-atlases/cdbs/calspec/
[11] http://irtfweb.ifa.hawaii.edu/~spex/IRTF_Spectral_Library/
[12] http://irtfweb.ifa.hawaii.edu/~spex/IRTF_Extended_Spectral_Library/
[13] http://xsl.astro.unistra.fr/index.html

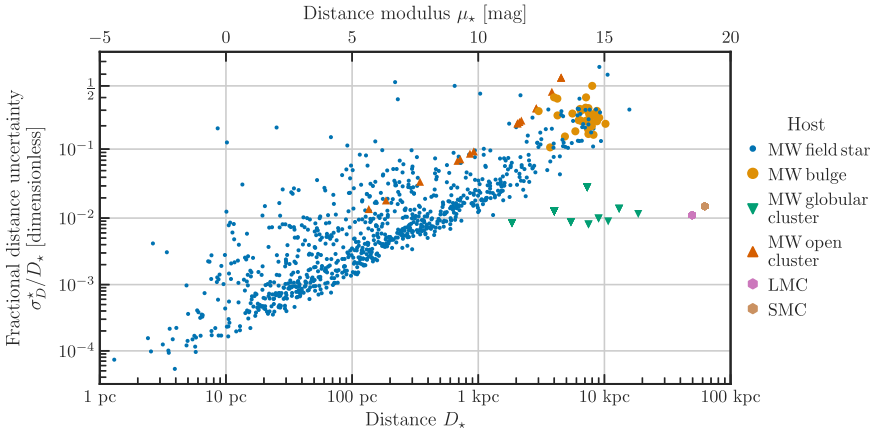

Figure 2. Fractional distance uncertainties as a function of distance (linear on the lower axis, modulus on the upper) for all library stars. Colors and symbols correspond to host objects, which are Galactic field or bulge stars, open and globular clusters, and the Magellanic Clouds. Note that many of the distance uncertainties are asymmetric; we show the mean values here.

available membership data, we supersede the Bailer-Jones et al. (2021) distance if the median cluster membership probability is greater than 50%. For nine candidates without membership data, we compare individual Bailer-Jones et al. (2021) distances to those derived for the parent clusters, and accept the cluster distances for all but two stars whose individual distances differ from the cluster distance by more than a factor of two.

For Magellanic Cloud stars, we do not require distance information to obtain reddening values, as two-dimensional (2D) extinction maps offer sufficient correction. For completeness, we adopt the detached eclipsing binary distances from Pietrzyński et al. (2019; $m - M = 18.477 \pm 0.004 \pm 0.026$) and Graczyk et al. (2020; $m - M = 18.977 \pm 0.016 \pm 0.028$) for 51 and 25 stars in the Large and Small Magellanic Clouds, respectively.

For the remaining 34 stars without distances from any of these sources, 14 have parallax distances from Gaia DR2 (Bailer-Jones et al. 2018), and 13 from Hipparcos (van Leeuwen 2007). Seven have distances derived from various other methods, primarily luminosity fitting (Sahai et al. 2007; Schmidt et al. 2010; Torres et al. 2010; Davies & Beasor 2020; Maíz Apellániz et al. 2022).

We were unable to locate any literature distance information for only one star, UCAC2 18505584. As this star is toward the Galactic bulge, we conservatively assume its distance is 8 ± 4 kpc.

In summary, distances for 894 stars were adopted from Bailer-Jones et al. (2021), 57 stars from cluster distances, 76 from Magellanic Cloud eclipsing binary distances, and 34 from other sources.

Figure 2 shows the average fractional distance uncertainties ($\sigma_D^\star/D_\star$) against distance moduli ($\mu_\star$) for our preferred distances for all library stars. Many of these distances have asymmetric upper and lower uncertainties; we describe how we incorporate asymmetric distance uncertainties into our star-by-star $E(B-V)$ estimates where possible in Section 2.2.2. For Galactic field and bulge stars, uncertainty largely scales with distance, as expected. The best measured of these have a less than 1% distance uncertainty out to ∼1 kpc, and 10% at ∼10 kpc. The uncertainties on open cluster distances scale similarly, as we adopt the most conservative reported uncertainties based on assumed parallax offsets of $\Delta\omega = \pm 0.1$ mas (Cantat-Gaudin & Anders 2020). The globular cluster distances of Baumgardt & Vasiliev (2021), on the other hand, incorporate information from multiple distance determination techniques wherever available, of which parallax inversion is only one. Several of these distances reach 1% uncertainty out to ∼10 kpc, and all are within 5%. Finally, the detached eclipsing binary distances to the Large and Small Magellanic Clouds have 1%–2% formal uncertainties. These are almost certainly underestimates for individual stars given line-of-sight depth variations, especially in the Small Magellanic Cloud (Ripepi et al. 2017, 2022, and references therein). However, the larger distance uncertainties are not a concern for reddening corrections, as the Magellanic Cloud reddening map is distance independent.

2.2.2. Reddenings

With distances in hand, we can now obtain line-of-sight reddening estimates for our sample. For the majority of the Galactic disk and bulge stars, including cluster stars, we use the 3D all-sky map from Vergely et al. (2022),[14] which uses a hierarchical inversion algorithm to derive line-of-sight extinctions over a $10 \times 10 \times 0.8$ kpc volume around the Sun to stars with high-quality Gaia EDR3 parallaxes and Gaia and 2MASS photometry. This map revises Lallement et al. (2022) with an improved calibration for cool giant stars specifically, and Lallement et al. (2022) itself updates Lallement et al. (2019). We use this map for 808 stars in total.

For the 178 Galactic stars that fall outside the boundaries of the Vergely et al. (2022) map, we use the Gaia DR3 total Galactic extinction (TGE) map (Delchambre et al. 2023). This map combines individual extinction measurements inferred from low-resolution BP/RP spectra (Andrae et al. 2023) of giants outside the Galactic plane ($|b| > 300$ pc or Galactocentric radius $R > 16$ kpc).

Finally, for Magellanic Cloud stars we use the 2D map presented by Skowron et al. (2021), which is derived from the Optical Gravitational Lensing Experiment (OGLE)-IV red clump color excess measurements.

We show the spatial distribution of adopted reddenings for our full sample in Figure 3, with respect to Galactic coordinates in three distance bins for Milky Way stars, and with respect to equatorial coordinates for the Magellanic Clouds. As expected, the majority of heavily reddened stars are found in the Galactic

[14] Available at https://explore-platform.eu/sdas.

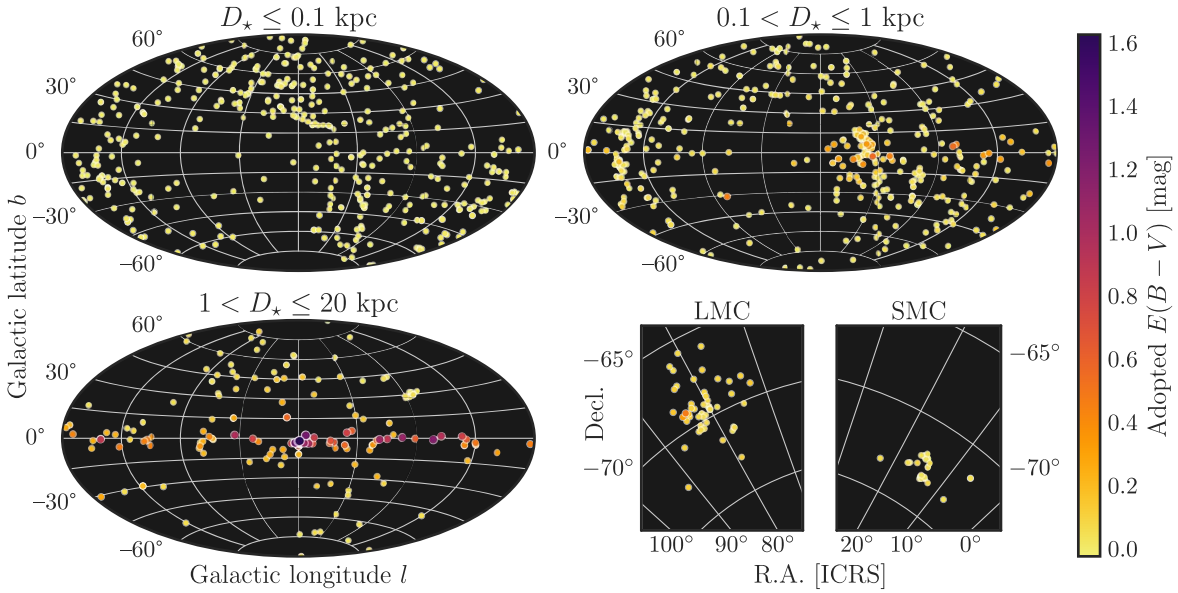

Figure 3. Sky maps of our final cross-library sample, color coded by adopted $E(B-V)$ values. We show all-sky maps in Galactic coordinates for Milky Way stars in three distance bins of 0–0.1 kpc, 0.1–1 kpc, and 1–20 kpc. Magellanic Cloud stars are shown in separate insets in the lower right in equatorial coordinates.

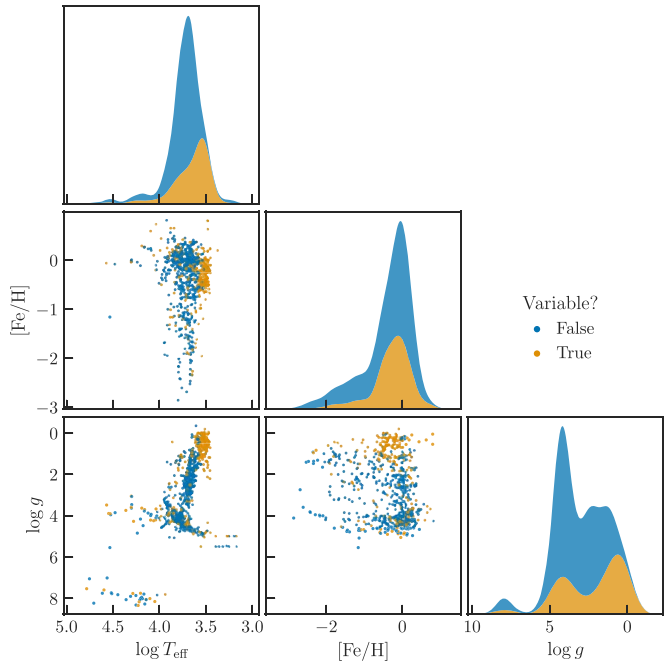

Figure 4. Summary stellar properties (effective temperature $T_{\rm eff}$, metallicity [Fe/H], and surface gravity $\log(g)$) of the merged spectral libraries. We note that these literature measurements are extremely heterogeneous, and these data are used primarily to understand the ranges of stellar properties over which our library can provide insight. Stars with known photometric variability are plotted in orange, whereas stars not known to be variable are shown in blue.

plane at distances beyond 1 kpc. In Appendix B we compare our final adopted $E(B-V)$ values both to those adopted or measured by the original libraries, and to those from several other widely used maps and stellar parameter fitting techniques. We find that different $E(B-V)$ estimates have typical median absolute deviations (MADs) of 0.05–0.1 mag, with some exceptions. This translates to a ∼2%–5% MAD in $E(J-K_S)$, assuming $E(J-K_S)/E(B-V) = 0.42$ (Yuan et al. 2013).

A similar intercomparison of the values from Skowron et al. (2021) with other such measurements in the Magellanic Clouds

Table 2
Summary of Gaia (E)DR3 and 2MASS Observed and Synthetic Photometry Differences for CALSPEC Stars, Following the Method of MA18 and References Therein

Band		ΔZP	σ(ΔZP)	$\bar{\sigma}_{\rm obs}$	$\bar{\sigma}_{\rm syn}$	$N_\star$
Gaia	BP	0.0175	0.0052	0.0030	0.0042	80
	G	0.0184	0.0068	0.0028	0.0042	82
	RP	0.0208	0.0052	0.0039	0.0045	80
2MASS	J	–0.0030	0.0229	0.0248	0.0085	45
	H	0.0283	0.0172	0.0258	0.0099	30
	K_S	0.0168	0.0176	0.0244	0.0116	23

Note. ΔZP and σ(ΔZP) are the error-weighted mean and standard deviation of the zero-point (ZP) differences (in the direction observed – synthetic); $\bar{\sigma}_{\rm obs}$ and $\bar{\sigma}_{\rm syn}$ are the respective mean uncertainties; and $N_\star$ is the number of stars used.

(e.g. Imara & Blitz 2007; Haschke et al. 2011; Choi et al. 2018; Bell et al. 2019; Joshi & Panchal 2019; Chen et al. 2022) would be of potential interest as well. We do not pursue it here because the proportion of Magellanic Clouds stars in our sample is low (below 10%), and many of those spectra are affected by data quality issues regardless.

2.3. Global Sample Properties

In addition to distances and reddenings, we have compiled relevant literature data for our sample from Vizier and SIMBAD. These include stellar parameters such as effective temperature $T_{\rm eff}$, metallicity [Fe/H], and surface gravity $\log(g)$; observed Gaia and 2MASS photometry; spectral type and other classifications; and binarity and variability information. We show a summary of $T_{\rm eff}$, $\log(g)$, and [Fe/H] coverage in Figure 4.

3. Synthetic Photometry

Here we describe the process of producing and validating synthetic photometry from our ensemble library. For ease of reproducing or expanding on this work, all derived products have been made public; we describe those data in Appendix A.

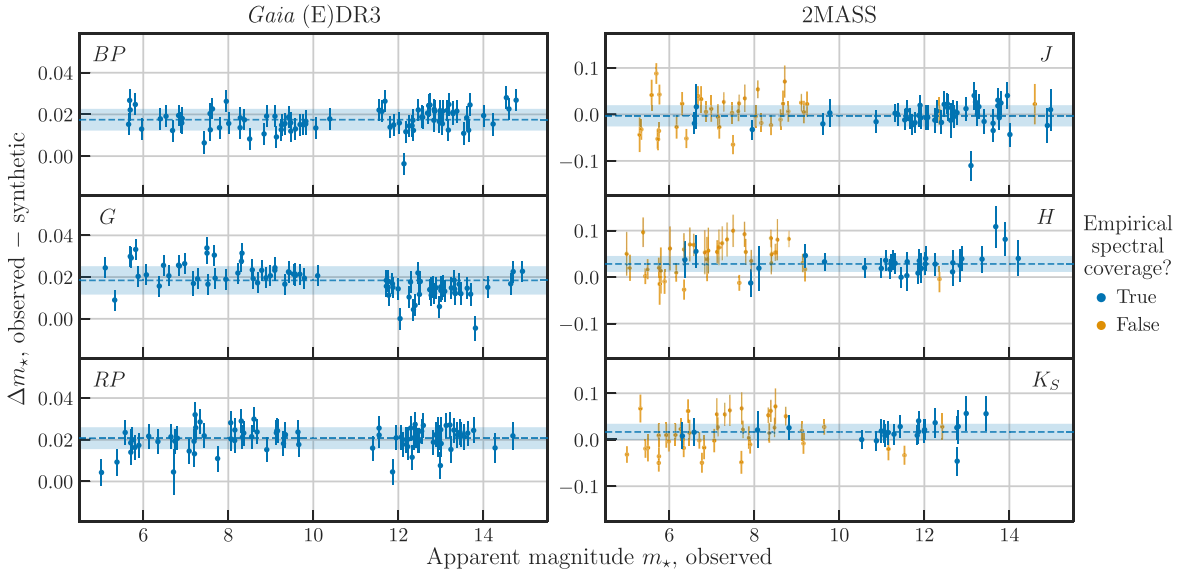

Figure 5. Differences between observed and synthetic magnitudes in Gaia (E)DR3 BP, G, and RP (left) and 2MASS JHK_S (right) as functions of observed magnitude for select CALSPEC stars. Blue points indicate empirical spectrophotometry (available for effectively all CALSPEC stars in the optical), and orange indicates spectra extrapolated from theoretical models (e.g. missing WFC3/IR and/or NICMOS data), which we exclude from calculations and show only for reference. Blue dashed lines and solid bands show the weighted means and standard deviations of the photometric offsets, as reported in Table 2.

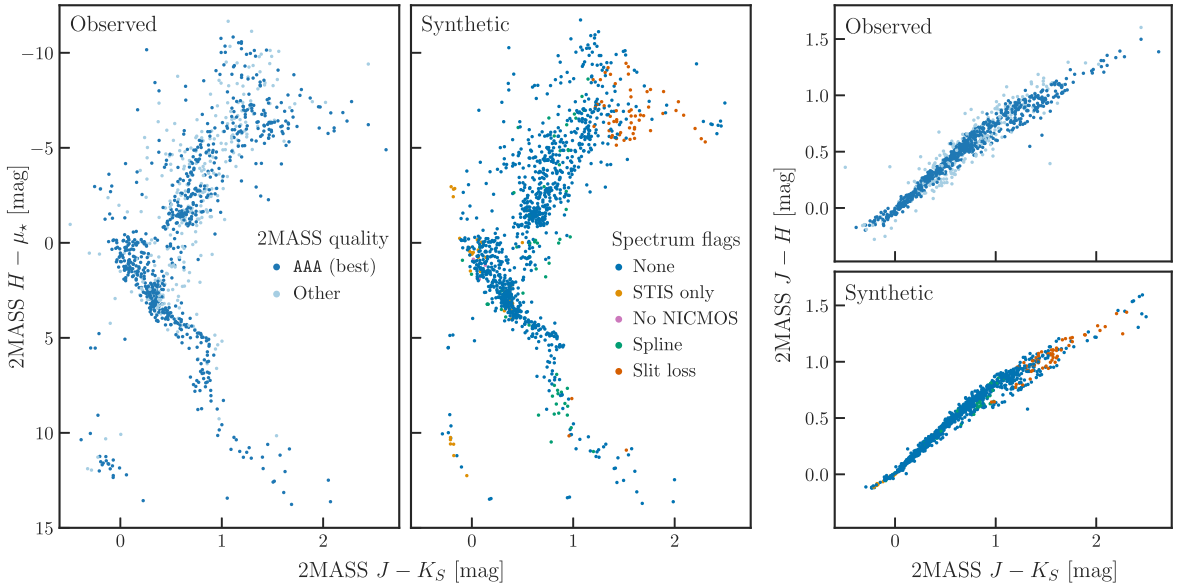

Figure 6. Left: absolute H vs. $J - K_S$ CMD of all available 2MASS photometry for our full sample. Here, dark blue points indicate sources with high-quality 2MASS photometry in all bands (`Qflg=AAA`) and light blue indicates nonoptimal quality flags in one or more bands. Center: the same CMD for our synthetic photometry suite. Blue points indicate spectra with no data caveats. Orange indicates CALSPEC library stars that were observed only with STIS, where the spectra are filled in outside the STIS wavelength range ($\gtrsim$1 μm) using theoretical spectra. Green indicates XSL spectra that were corrected for slit loss via spline fitting (Verro et al. 2022b), and red indicates XSL spectra uncorrected for slit loss. Right: the same in $J - H$ vs. $J - K_S$ color–color space.

3.1. Synthetic Photometry Procedure

For a given spectrum with flux density $f_\lambda(\lambda)$ and bandpass with dimensionless throughput $P(\lambda)$, the integrated flux density is defined as:

$$f_\lambda(P) \equiv \frac{\int f_\lambda(\lambda) P(\lambda) \lambda \, \mathrm{d}\lambda}{\int P(\lambda) \lambda \, \mathrm{d}\lambda}, \tag{1}$$

(Strömgren 1937; Koornneef et al. 1986).

If we treat the spectrum $f_\lambda(\lambda)$ as a vector $\boldsymbol{f}_\lambda$, and a set of bandpasses $\boldsymbol{P}$ as a matrix with dimensions $n_P \times n_\lambda$, where n_P is the number of bandpasses and n_λ is the number of wavelength samples, then the integrated fluxes $\boldsymbol{f}_P$ are simply:

$$\boldsymbol{f}_P = \boldsymbol{P} \cdot \boldsymbol{f}_\lambda. \tag{2}$$

This approach allows us to calculate the covariance between integrated fluxes in different bandpasses as:

$$\mathrm{Cov}[\boldsymbol{f}_P] = \boldsymbol{P} \cdot \mathrm{Cov}[\boldsymbol{f}_\lambda] \cdot \boldsymbol{P}^T, \tag{3}$$

following Gaia Collaboration et al. (2023).

We begin by resampling all spectra and transmission curves to the $R = 100$ wavelength grid on which the HST flux uncertainty scale is defined (Bohlin et al. 2014), to improve

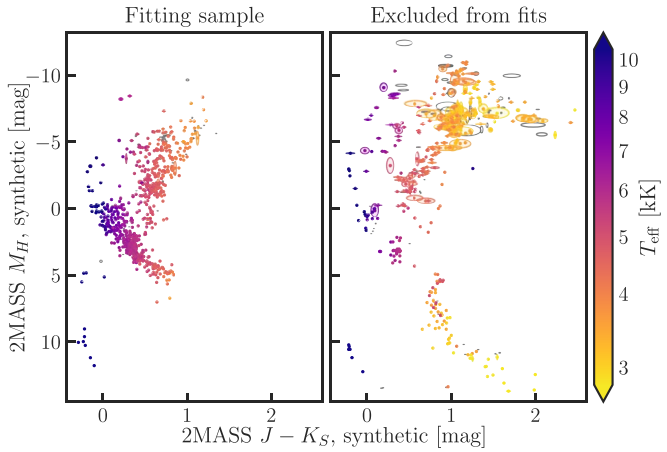

Figure 7. CMDs of our final fitting sample (left) and stars excluded from fitting (right), color mapped by literature effective temperature.

computational efficiency and ease of uncertainty propagation. We used the `FluxConservingResampler` from the Python package `specutils`, which preserves integrated flux and associated uncertainties (Carnall 2017). For XSL spectra, we first fill in the deepest telluric-dominated regions (1.35–1.41 and 1.81–1.935 μm) via convolution with a Gaussian kernel.

Next, we correct the resampled spectra for interstellar extinction. Specifically, we estimate the total wavelength-dependent line-of-sight extinction A_λ using the $E(B-V)$ values described in Section 2.2.2 as inputs to extinction laws implemented in the `dust-extinction` package.[15] We use the Fitzpatrick et al. (2019) law with $R_V = 3.1$ for Galactic stars, and in the Large Magellanic Cloud and Small Magellanic Cloud we use the respective average laws from Gordon et al. (2003). We incorporate both the reported uncertainties on $E(B-V)$ and, in the Galactic case, uncertainties of ± 0.3 on R_V into the final uncertainties on the deextinguished spectra.

Using Equations 2 and 3, we are able to derive integrated fluxes and covariances for an arbitrary set of bandpasses $\boldsymbol{P}$ over both the original and deextinguished spectra. For the remainder of this paper, we will focus primarily on the 2MASS JHK_S and HST WFC3/IR F110W, F125W, and F160W bandpasses. However, we also provide synthetic Gaia DR3 *BP*, *G*, and *RP* magnitudes for spectra with sufficient wavelength coverage in this paper. Comparable sets of transformations for JWST/NIRCam, Roman/WFI, and other ground-based systems will be presented in a follow-up paper.

In this work we use throughput data provided under the HST calibration reference data system (CRDS)[16] context `hst_synphot_0055.imap`. For HST these include a number of telescope and instrument component files which may be assembled into full-system throughputs using the `stsynphot` Python package (STScI Development Team 2020). The WFC3 implementation offers options to specify an observation date and aperture radius, which modify the net throughputs using encircled energy and time-dependent sensitivity information (Hartig 2009; Calamida et al. 2022); here we use the default "infinite" (6.″0) aperture and instrument reference epoch MJD = 55,008. The canonical 2MASS relative spectral response curves (Cohen et al. 2003) are also provided in CRDS for use with `stsynphot`. The relevant transmission curve files are named `wfc3_ir_<band>_mjd_007_syn.fits` and `2mass_<band>_001_syn.fits`, respectively.

3.2. Validation

Overall, the best check on synthetic magnitudes and colors is to compare them to corresponding measured values. In this section, we first cross-check our CALSPEC data against high-quality 2MASS and Gaia photometry, and then consider the global 2MASS color–magnitude and color–color fidelity of the full sample.

3.2.1. CALSPEC Zero-points

While an end-to-end recalibration in either direction (as in, e.g., Riess 2011; Maíz Apellániz & Weiler 2018; Maíz Apellániz & Pantaleoni González 2018; Gaia Collaboration et al. 2023) is beyond the scope of this paper, here we briefly reproduce the 2MASS zero-point adjustment procedure of Maìz Apellàniz & Pantaleoni Gonzal`ez (2018; hereafter MA18) and references therein. We extend this procedure to Gaia (E)DR3 as well for additional verification, as in Fabricius et al. (2021, their Section 4.4.2).

We choose our comparison sample based on the criteria of MA18 with minor updates, namely: (a) CALSPEC spectra with empirical IR spectrophotometry (limited to NICMOS in MA18; here we also include WFC3/IR) and (b) uncertainties on observed magnitudes of 0.05 mag or less. For Gaia, we use all available CALSPEC stars with observed magnitudes $5 < m_\star < 15$. All criteria are applied on a per-band basis.

We calculate mean offsets and dispersions weighted by combined synthetic and observed magnitude uncertainties for each band, as summarized in Table 2 and shown in Figure 5. We find a consistent $\sim$0.02 mag offset between the synthetic and observed photometry in all Gaia bands, and offsets of up to 0.03 mag in 2MASS, although the latter are all statistically compatible with zero. We attribute these largely to differences in the respective adopted reference SEDs, consistent with previous studies of synthetic Gaia and 2MASS magnitudes (MA18; Casagrande & VandenBerg 2018) and historical changes to the CALSPEC Vega calibration (Bohlin et al. 2014, 2019).

3.2.2. Global CMD and Color–Color Fidelity

Figure 6 compares the absolute observed 2MASS magnitudes (left) to their synthetic counterparts (right) in a M_H versus $J-H$ color–magnitude diagram (CMD). The right panel of Figure 6 separates the highest-quality photometry, `Qflg` = `AAA` (Skrutskie et al. 2006), from that with flags in one or more bands; the best photometry is shown as dark blue, and the lower quality in lighter blue. Visually, the stars with lower photometric quality have larger scatter around prominent CMD features (e.g., the RGB, main sequence, and white dwarf cooling sequence) that are tightly traced by the high-quality photometry.

The left panel of Figure 6 uses our synthetic magnitudes, where the points are color coded if there are quality flags within the spectral libraries themselves. Of note: the orange points are CALSPEC stars observed only with STIS, meaning that the spectrum beyond $\sim$1 μm is synthetic (Bohlin et al. 2017); the green are XSL spectra corrected for slit-dependent flux loss with a spline function (Verro et al. 2022b); and the red are XSL spectra uncorrected for slit loss.

[15] https://web.archive.org/web/20230706195114/https://learn.astropy.org/tutorials/color-excess.html
[16] https://hst-crds.stsci.edu/

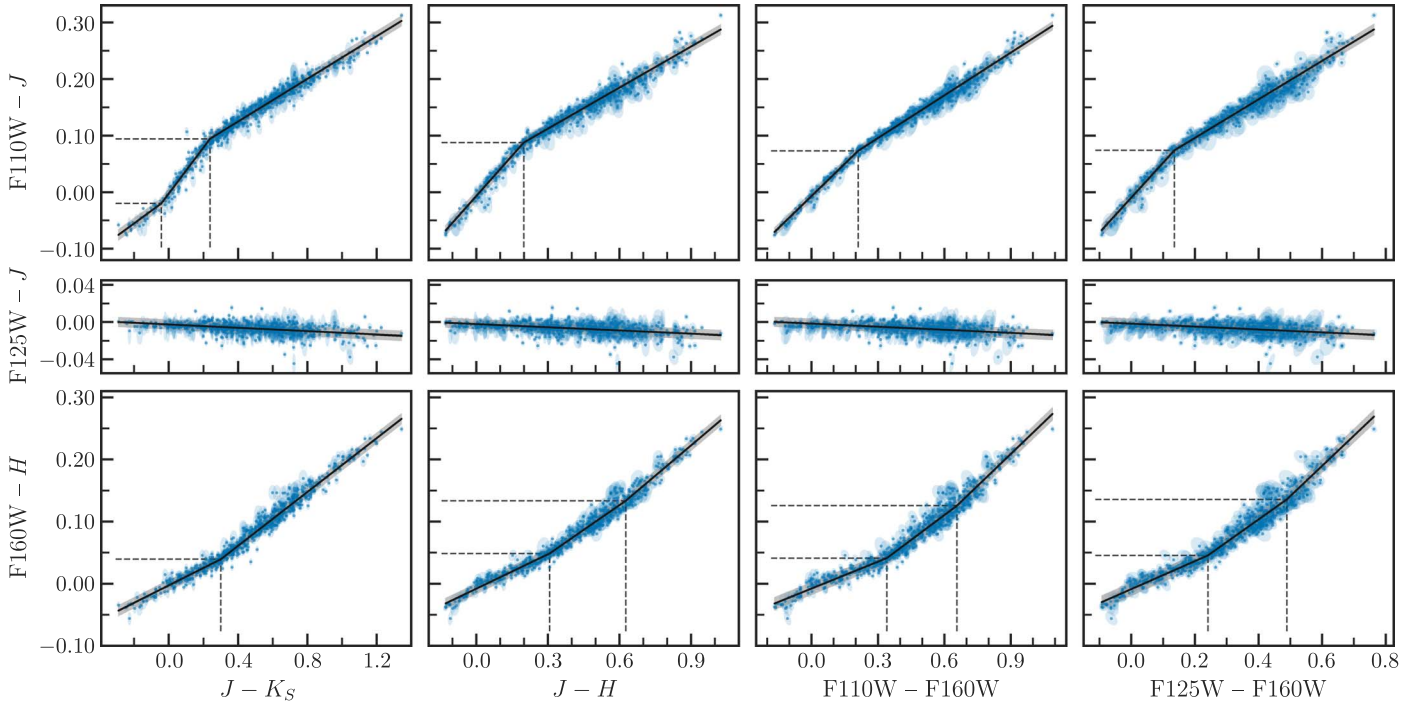

Figure 8. Filter transformation fits to F110W – J (top row), F125W – J (center row), and F160W – H (bottom row) as functions of $J - K_S$, $J - H$, F110W – F160W, and F125W – F160W color from left to right. Points used in the fitting are shown in dark blue with light blue covariance ellipses. Solid black lines show the resulting piecewise linear transformations with 68% confidence intervals in gray, and dashed black lines mark the break-point locations.

Table 3
Filter Transformation Results

Y	X	X_0	X_1	c_0	c_1	$\sigma_{\rm seg}$	$N_\star$	$\sigma_{\rm fit}$
F110W – J	$J - H$	−0.13	0.20	−0.0066	0.4743	0.0091	153	0.0088
		0.20	1.02	0.0396	0.2419	0.0087	620	”
	$J - K_S$	−0.29	−0.04	−0.0103	0.2244	0.0078	29	0.0088
		−0.04	0.24	−0.0025	0.4065	0.0117	137	”
		0.24	1.34	0.0494	0.1885	0.0080	607	”
	F110W – F160W	−0.17	0.21	−0.0069	0.3797	0.0059	125	0.0073
		0.21	1.09	0.0200	0.2518	0.0075	648	”
	F125W – F160W	−0.09	0.14	−0.0096	0.6162	0.0090	128	0.0093
		0.14	0.76	0.0278	0.3404	0.0094	645	”
F125W – J	$J - H$	−0.13	1.02	−0.0023	−0.0115	0.0050	773	0.0050
	$J - K_S$	−0.29	1.34	−0.0027	−0.0090	0.0051	773	0.0051
	F110W – F160W	−0.17	1.09	−0.0018	−0.0111	0.0051	773	0.0051
	F125W – F160W	−0.09	0.76	−0.0018	−0.0156	0.0051	773	0.0051
F160W – H	$J - H$	−0.13	0.31	−0.0080	0.1845	0.0063	268	0.0081
		0.31	0.63	−0.0330	0.2659	0.0089	386	”
		0.63	1.02	−0.0704	0.3256	0.0094	119	”
	$J - K_S$	−0.29	0.30	−0.0027	0.1402	0.0064	217	0.0082
		0.30	1.34	−0.0257	0.2166	0.0089	556	”
	F110W – F160W	−0.17	0.34	−0.0079	0.1442	0.0076	224	0.0096
		0.34	0.66	−0.0496	0.2668	0.0100	407	”
		0.66	1.09	−0.0992	0.3424	0.0113	142	”
	F125W – F160W	−0.09	0.24	−0.0087	0.2253	0.0074	246	0.0102
		0.24	0.49	−0.0420	0.3634	0.0108	409	”
		0.49	0.76	−0.1022	0.4864	0.0131	118	”

Note. Filter transformations take the functional form $Y = c_0 + c_1 X$ for $X_0 < X \leqslant X_1$, where X is a broadband color and Y is the difference between comparable filters. $\sigma_{\rm seg}$ is the weighted rms dispersion of the residuals in each segment (e.g., with $X_0 < X \leqslant X_1$), and $\sigma_{\rm fit}$ is the same for the full piecewise relation. $N_\star$ is the number of stars per segment.

Generally, the scatter in the right panel of Figure 6 is reduced with the synthetic photometry, which is a comforting check on our processes. However, we emphasize that the absolute-scale synthetic magnitudes for XSL in particular should be treated with caution, as the XSL spectra are calibrated only for relative (wavelength-dependent) flux and not absolutely fluxed. We do

not make more detailed comparisons here because of the relatively large sample of stars known to be variable, particularly on the upper giant branch (e.g., Figure 4) and the comparison here would likely only serve to highlight cases where the spectra and photometry were taken at inconsistent phase points.

4. Results

4.1. Fitting Sample Selection

To construct general-purpose filter transformations, we require a subset of library stars with high-quality spectra covering as broad a swath of the H-R diagram as possible. Given the heterogeneity of available information for stars in our library, we combine several complementary kinds of classification data to accept or reject stars for our final calibration sample. We selected the fitting sample based on the following criteria:

1. Synthetic magnitude uncertainties under 0.05 mag in all bands;
2. No spectral quality flags (see Figure 6);
3. No known atypical SED features, based on available SIMBAD object class and spectral type information. Specifically, we reject stars with any of the following literature classifications:
   (a) Ae or Be stars, which often show IR excesses from circumstellar decretion disks;
   (b) Dwarfs of type M or later, including L and T dwarfs;
   (c) C-, R-, and S-type stars; these are mainly AGB stars of varying masses, but also include carbon-enhanced metal-poor and other chemically peculiar non-AGB stars;
   (d) Other extreme giant types, including Miras, OH/IR and post-AGB stars, and supergiants of any temperature;
   (e) Any other stars with $T_{\rm eff} < 3500$ K.

Together, these yield a sample of 773 high-quality spectra of 648 unique stars in total. CMDs of accepted and rejected stars are shown in Figure 7. The fitting sample is dominated by main-sequence and RGB stars the color range $-0.3 < J - K_S < 1.35$.

4.2. Fitting Process

We plot differences between comparable HST and 2MASS magnitudes as functions of color for our fitting sample in Figure 8. In general, they follow consistent and well-defined relations, albeit not necessarily linear ones.

Deviations from linearity are most clearly seen in F110W – J versus $J - K_S$ (the upper leftmost panel of Figure 8). Here, the noticeably steeper slope at $0 \lesssim J - K_S \lesssim 0.25$ corresponds to the 0.82 μm Paschen jump, which is strongest in A-type stars (Taylor 1986; Straizys 1998). The slope change at the blue end of this feature is only detectable in F110W – J versus $J - K_S$, as F110W is the most blue-sensitive filter and $J - K_S$ the widest available color baseline. However, we consistently observe slope changes at colors of about 0.2 to 0.35 mag in F110W – J and F160W – H for all color baselines.

A more subtle change in F160W – H also appears near 0.5–0.65 mag for all colors except $J - K_S$. We attribute this to the 1.6 μm "bump," where the $H-$band continuum opacity reaches a minimum as the dominant absorption mode transitions from photoionization to free–free (John 1988; Allende Prieto 2023). This produces a well-defined peak in the cool stars' SEDs, which is strongest in intermediate M-type giants and supergiants (Rayner et al. 2009). The H band is nearly centered on this feature, but F160W falls about 0.1 μm blueward of its peak, resulting in slightly dimmer F160W magnitudes relative to H.

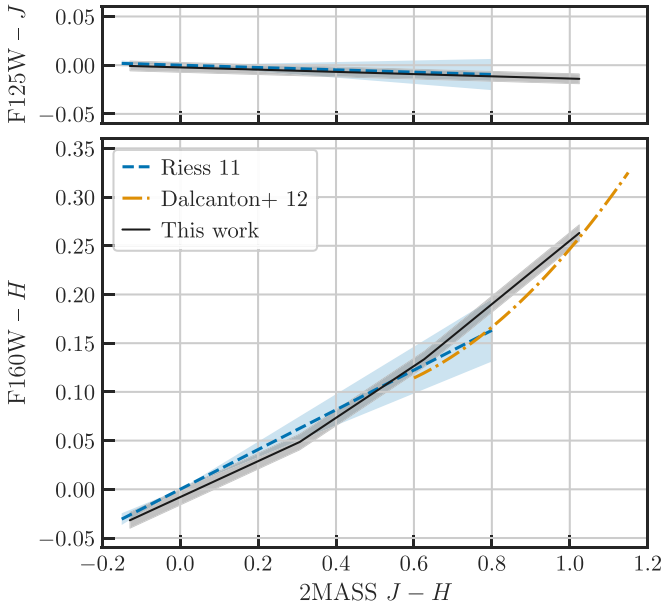

Figure 9. Comparisons to previously published transformations for F125W – J (Riess 2011; upper panel) and F160W – H (lower panel; Riess 2011 in blue; Dalcanton et al. 2012 in orange). Results of this work are shown in gray.

We fit transformations using the Python library `pwlf` (Jekel & Venter 2007), which solves for a system of piecewise linear equations continuous over the data domain.[17] The current version as of this writing, v0.2.0, offers the options to fit for optimal break-point locations given a desired number of line segments, and to incorporate weights in the least-squares regression. For a synthetic color X and HST – 2MASS magnitude difference Y, we weight by the inverse variance:

$$w_{X,Y}^{-2} = \sigma_X^2 + \sigma_Y^2 - \mathrm{cov}(X, Y), \quad (4)$$

where cov(X, Y) is obtained by propagating the uncertainties from Equation (3).

Our fitting results are summarized in Table 3, and over-plotted in black in Figure 8.

5. Discussion

5.1. Comparison with Literature Relations

Earlier works have carried out similar exercises to what we have done here using theoretical stellar atmospheres.

Riess (2011) derived first-order transformations between F125W, F160W, and JH as part of an investigation of the WFC3/IR count rate nonlinearity (also known as reciprocity failure). They used the synthetic photometry from Castelli & Kurucz (2003) model atmospheres with $-0.15 < J - H < 0.8$, $T_{\rm eff} \geqslant 3500$ K, $\log(g) = 4.5$, and solar metallicity and

[17] For a detailed description of the `pwlf` algorithm and implementation, please see https://web.archive.org/web/20211203035946/https://jekel.me/2018/Continous-piecewise-linear-regression/. The original description of the method may be found at https://web.archive.org/web/20171116164225/https://www.golovchenko.org/docs/ContinuousPiecewiseLinearFit.pdf.

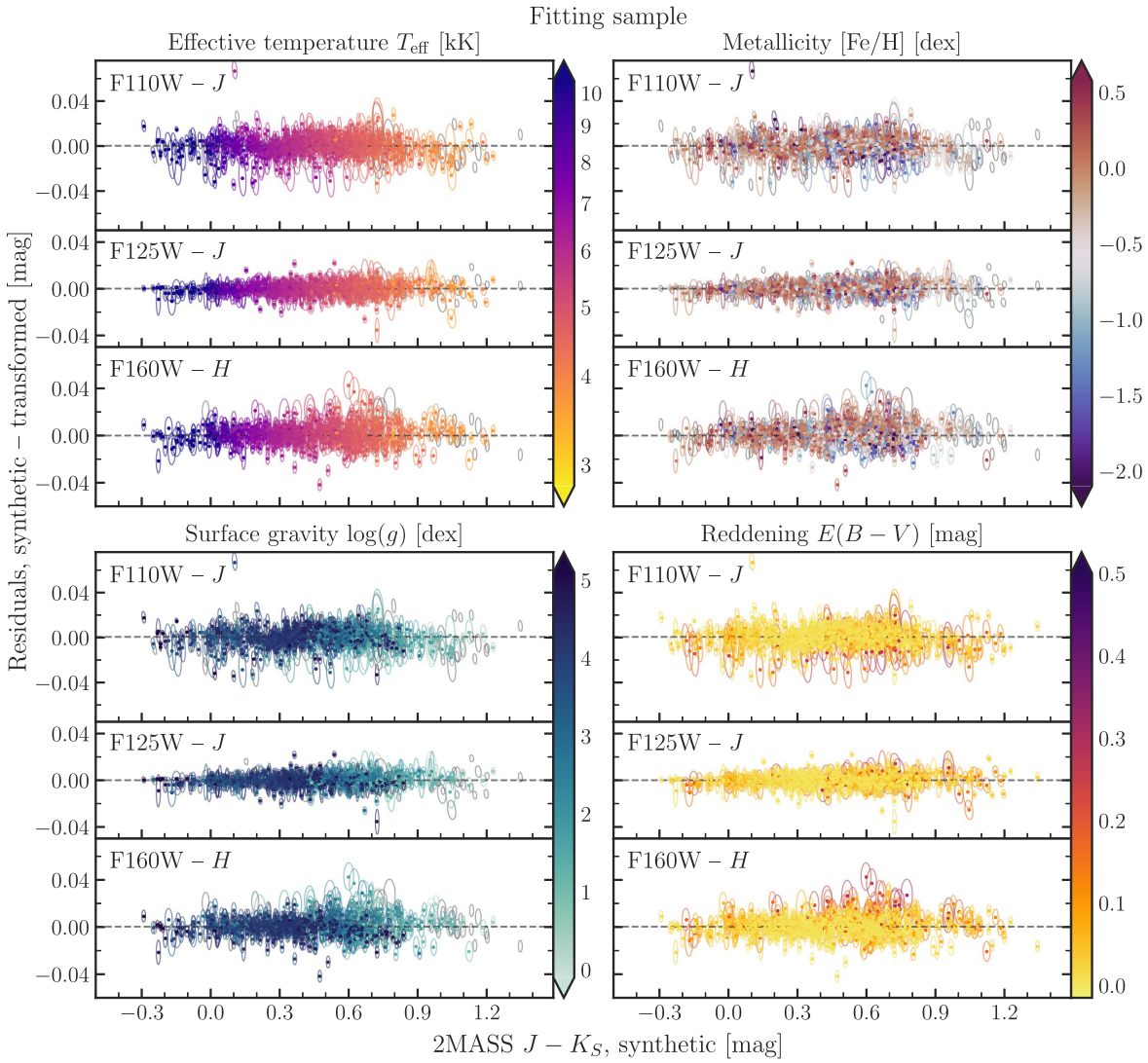

Figure 10. Residuals of our HST–2MASS filter transformations with respect to the $J-K_S$ color for our fitting sample (773 spectra of 648 unique stars). Color maps show relevant stellar parameters where available, including effective temperature $T_{\rm eff}$, metallicity [Fe/H], surface gravity log(g), and reddening $E(B-V)$. Reddenings are as described in Section 2.2.2; all other parameters are adopted as is from the literature sources.

abundance ratios. With these they fit the following color terms:

$$J - \mathrm{F125W} = +0.012(\pm0.020)(J-H), \quad (5)$$

$$H - \mathrm{F160W} = -0.204(\pm0.040)(J-H). \quad (6)$$

To interpret tip of the red giant branch (TRGB) color–magnitude absolute calibrations, Dalcanton et al. (2012) derived transformations using Padova isochrone predictions (Girardi et al. 2008) for 10 Gyr stars at the TRGB with $0.6 < J-H < 1.15$. Within this color range, the model transformations between JH and F110W, F160W were fit by:

$$\mathrm{F160W} - H = 0.2031 + 0.401(J-H-0.9) + 0.3498(J-H-0.9)^2, \quad (7)$$

$$J - H = 0.9418 + 0.841(\mathrm{F110W} - \mathrm{F160W} - 1.0) - 0.9053(\mathrm{F110W} - \mathrm{F160W} - 1.0)^2. \quad (8)$$

We show comparisons between Equations (5)–(7) and our results in Figure 9. We find overall excellent agreement with Riess (2011) in both bands, and only a very slight offset relative to Dalcanton et al. (2012) in F160W – H (∼0.02 mag at $J-H=0.8$, but less at both bluer and redder colors).

5.2. Stellar Properties

We now examine these transformations with respect to fundamental stellar properties. In Figure 10 through 13 we show the residuals of the transformations color coded by effective temperatures, surface gravities, and metallicities from the literature, as well as our adopted reddenings. Figures 10 and 11 show the residuals of our fitting sample, and Figures 10 and 11 show the residuals of stars excluded from the fits (i.e., those plotted in the right panel of Figure 7). Stars without literature parameters are shown as open gray covariance ellipses.

Figures 10 and 11 show that the fitting sample residuals are nearly all within 0.05 mag of our final filter conversions, and the majority are within 0.025 mag. However, there may also be slight differences in the residuals that correlate with stellar parameters, leading to either increased scatter or small biases that vary systematically with intrinsic quantities, like metallicity and surface gravity, or observed quantities like extinction. We note a possible metallicity dependence in the F110W – J and F160W – H residuals at $0.4 \lesssim J-H \lesssim 0.8$ (upper right of Figure 11), with metal-poor stars appearing to fall preferentially below the nominal fit (that is, slightly brighter in the HST filters

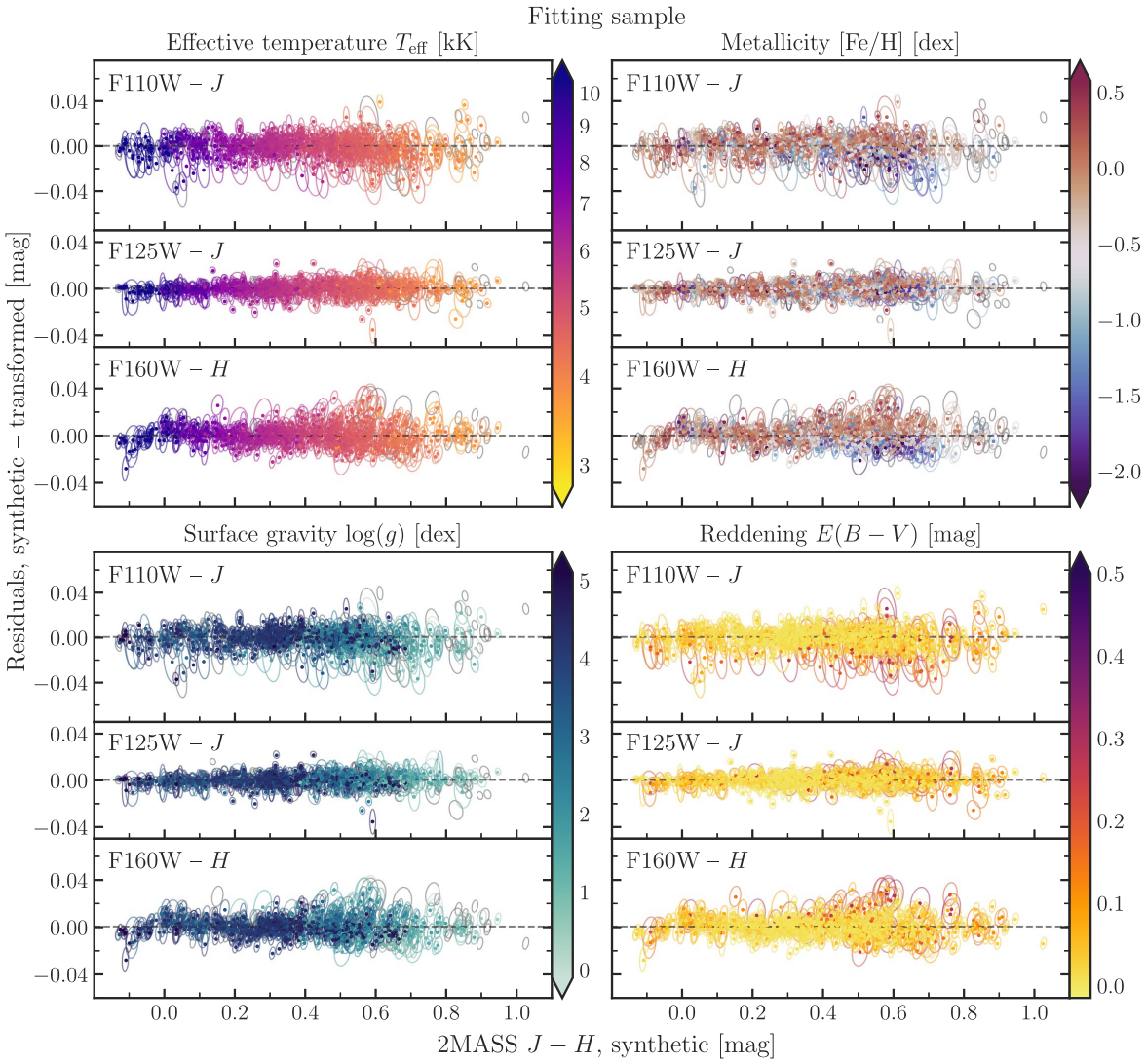

Figure 11. As Figure 10 with respect to the $J-H$ color on the x-axis.

relative to 2MASS than average), and metal rich above (dimmer in HST). This is more or less expected, as higher metal content generally reddens stellar spectra and F110W and F160W both fall blueward of J and H, respectively. However, we do not attempt to quantify this effect further given the heterogeneity of available metallicity information and possible confounding effects of surface gravity, dust, and/or specific abundance patterns such as alpha enhancement.

In the excluded sample (Figures 12 and 13), the most noticeable feature is the much higher level of scatter in the residuals overall, and the color dependence thereof. In particular, the residual amplitude increases dramatically for red stars ($J-K_S \gtrsim 1$ or $J-H \gtrsim 0.5$) due to deep absorption features and variability (see Figure 14).

5.3. Stellar Classifications

We now examine the residuals for several subclasses of luminous evolved stars, many of which are commonly used in the literature as primary distance indicators. Figure 14 compares synthetic photometry residuals for carbon-rich (blue) and oxygen-rich (orange) TP-AGB stars, RGB stars (green), RR Lyrae variables (RRL, red), and classical Cepheids (pink). For stars with multiple library spectra taken at different phase points, we connect their synthetic magnitudes with solid lines to show variability effects.

As seen for the reddest stars in the previous section, it is clear that TP-AGB stars show dramatically higher color–magnitude scatter relative to other stellar types due to temperature- and abundance-dependent absorption features. Furthermore, the strength of these features—as well as the overall SED shape—can vary significantly in individual stars over the course of a thermal pulsation cycle; indeed, we see changes in band-to-band residuals of up to ∼0.2 mag in several of the O-rich variables. We note that the XSL observations took simultaneous UV–optical–NIR spectra of such variables at multiple phase points to model their net effects on the integrated light of simple stellar populations accurately. These results highlight the need for similar observing strategies—and careful choices of filters—when cross-calibrating TP-AGB magnitudes between NIR photometric systems. This is especially salient in any distance-scale work that seeks to establish a common zero-point between local calibrators best observed from the ground (e.g. Galactic stars with trigonometric parallaxes or the Magellanic Clouds) and space-based extragalactic observations of distant galaxies.

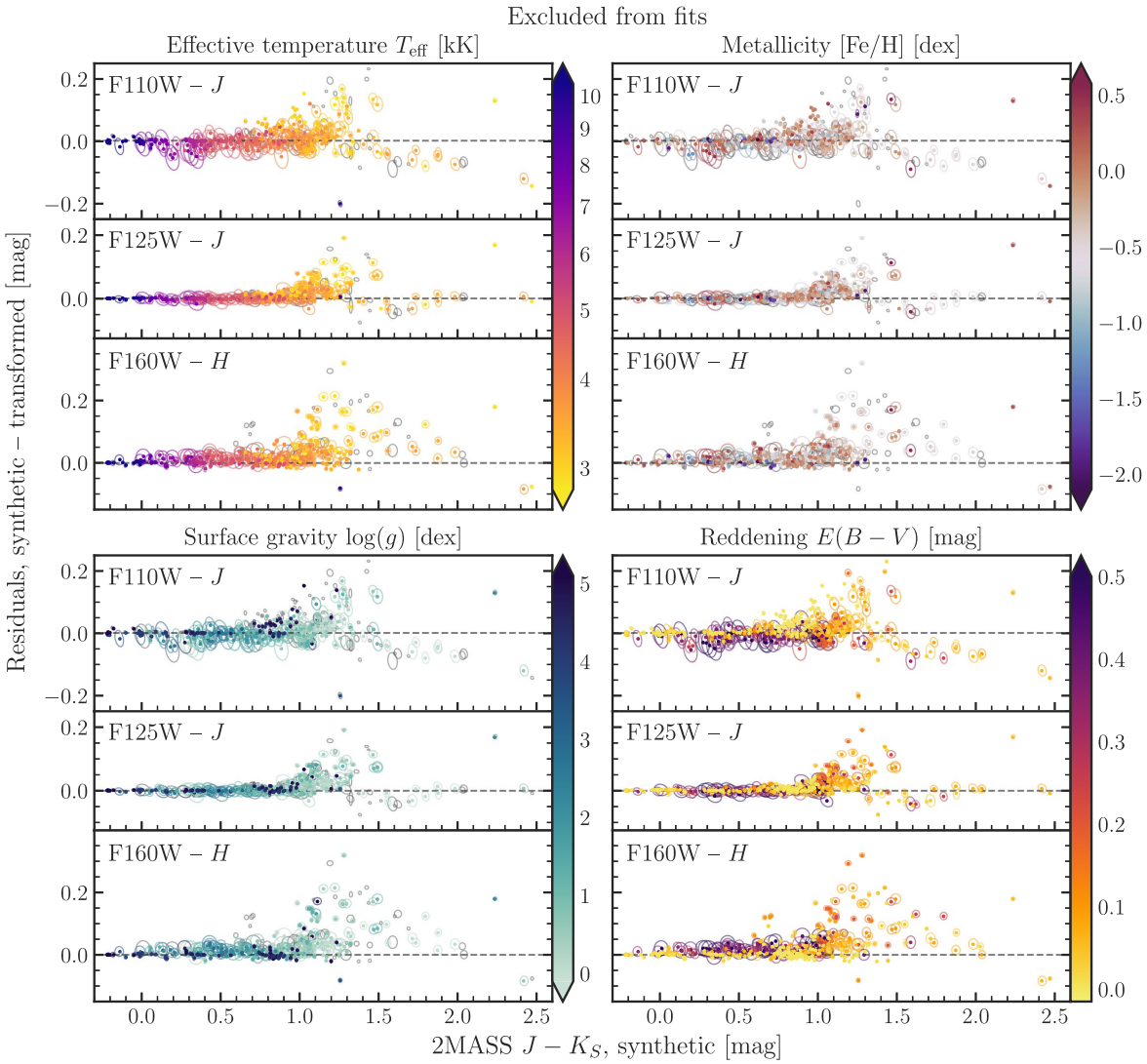

Figure 12. As Figure 10, but showing the residuals for stars excluded from our fitting sample (424 spectra of 643 unique stars). Note the changes in both the x- and y-axis ranges relative to Figures 10 and 11.

With the exception of the TP-AGB stars, however, we find that the transformations given in Table 3 hold well for RR Lyrae, Cepheids, and RGB stars, and require no additional uncertainties beyond those reported in Table 3.

6. Conclusions

We have derived new transformations between 2MASS and HST broadband filters based on synthetic photometry of empirical stellar spectra. While the majority of stars follow relations that are well constrained as a function of broadband color, stars with $T_{\rm eff} \lesssim 3500$ K in particular diverge significantly from these nominal relations due to molecular absorption. This is especially apparent in the case of both carbon- and oxygen-rich TP-AGB stars; furthermore, such stars' extreme and often irregular variability poses additional challenges for directly cross-calibrating them between systems. While we cannot recommend a one-size-fits-all set of transformations for these stars, readers may find the individual synthetic magnitudes and literature parameters compiled in Appendix A of use in this regard, depending on the application.

6.1. Future Work

We will use the data and methods presented here to predict similar transformations for a number of new and upcoming NIR photometric systems in a follow-up paper, including JWST/NIRCam, Roman/WFI, and Euclid/NISP.

While synthetic photometry is a well-tested and highly efficient method for predicting filter transformations, fully empirical calibrations are of course preferred when possible. In a future paper series (R. L. Beaton et al. 2023, in preparation), we will directly compare HST WFC3/IR spectrophotometry of cool giants in the Magellanic Clouds to JHK_S photometry of the same fields from the FourStar camera on Las Campanas Observatory's 6.5 m Baade telescope.

Acknowledgments

We thank the anonymous referee for comments which improved and clarified this paper. Support for this work was provided by NASA through HST program GO-15875. Support for this work was provided by the NSF through NSF grant AST-2108616. Support for some of this work was provided by NASA through Hubble Fellowship grant #51386.01 awarded

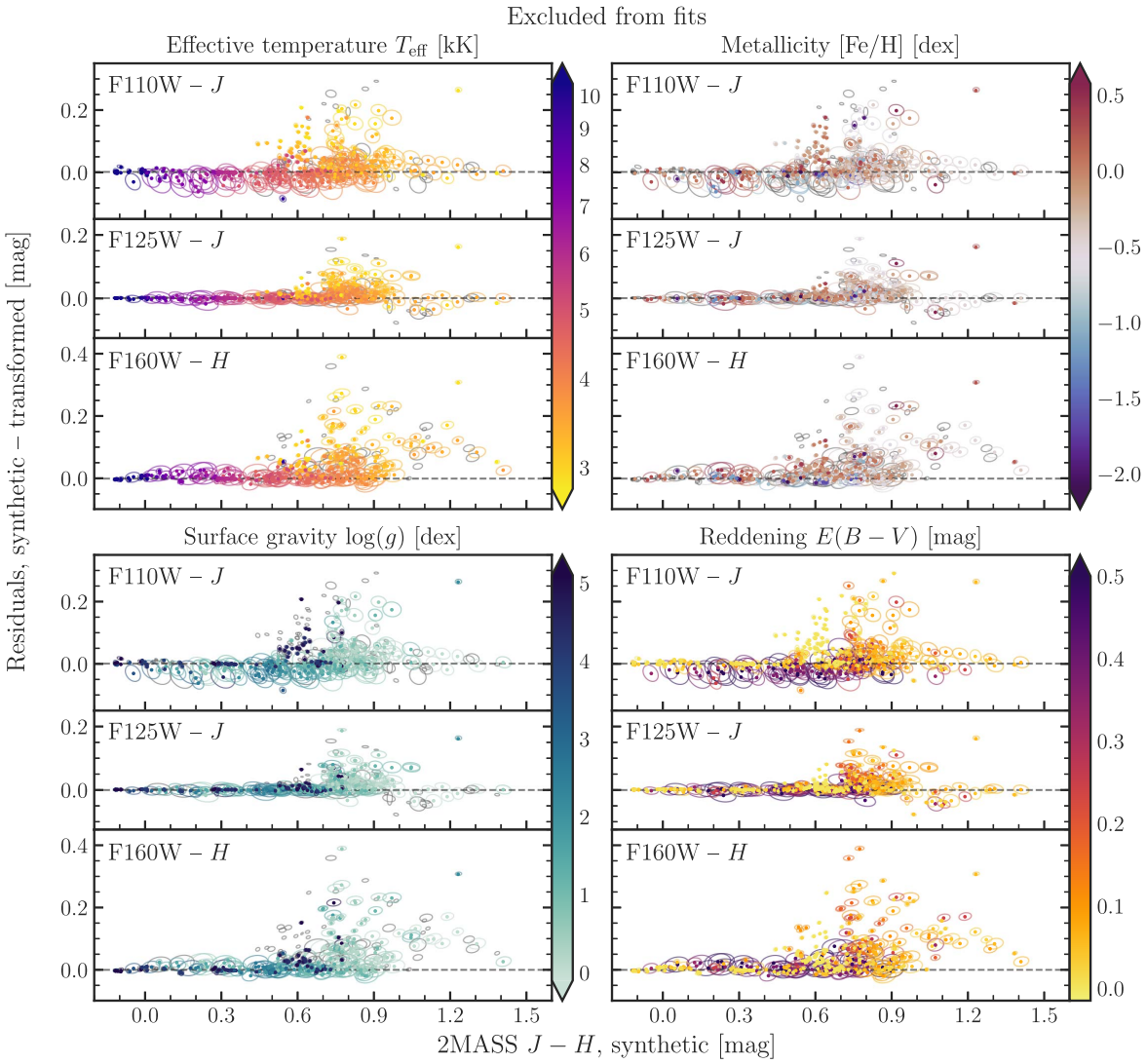

Figure 13. As Figure 12, with $J-H$ color on the x-axis. Again, note the differences in the x- and y-axis ranges between this and previous figures.

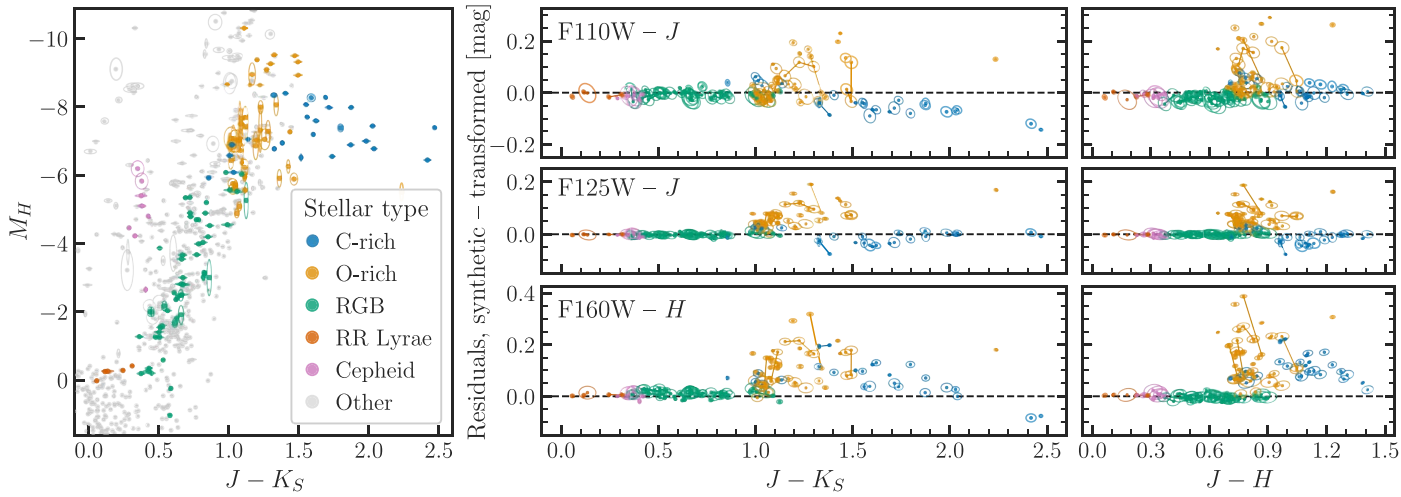

Figure 14. Synthetic 2MASS CMD (left) and filter transformation residuals (center, right) with several subtypes of evolved stars used as primary distance indicators highlighted by color. These include C- and O-rich TP-AGB variables in blue and orange respectively; first-ascent RGB stars in green; RR Lyrae variables in red; and classical Cepheids in pink. Repeat observations of the same stars are connected with solid lines.

to R.L.B. by the Space Telescope Science Institute, which is operated by the Association of Universities for Research in Astronomy, Inc., for NASA, under contract NAS 5-26555. We acknowledge the Undergraduate Summer Research Program (USRP) in the Princeton Department of Astrophysical Sciences that supported the initial work that formed this project; in

particular, the efforts of Peter Melchior and Polly Strauss. An early version of this work was presented as a Junior Paper to the Princeton Department of Physics and we thank Jo Dunkley and Lyman Page for their support as readers.

This research has made use of the SVO Filter Profile Service (http://svo2.cab.inta-csic.es/theory/fps/) supported from the Spanish MINECO through grant AYA2017-84089.

This publication makes use of data products from the Two Micron All Sky Survey, which is a joint project of the University of Massachusetts and the Infrared Processing and Analysis Center/California Institute of Technology, funded by the National Aeronautics and Space Administration and the National Science Foundation.

This work has made use of data from the European Space Agency (ESA) mission Gaia (https://cosmos.esa.int/gaia), processed by the Gaia Data Processing and Analysis Consortium (DPAC; https://cosmos.esa.int/web/gaia/dpac/consortium). Funding for the DPAC has been provided by national institutions, in particular the institutions participating in the Gaia Multilateral Agreement.

This research has made use of NASA's Astrophysics Data System.

This research has made use of the SIMBAD database, operated at CDS, Strasbourg, France. The original description of the SIMBAD service was published in Wenger et al. (2000).

This research has made use of the VizieR catalog access tool, CDS, Strasbourg, France (doi:10.26093/cds/vizier). The original description of the VizieR service was published in Ochsenbein et al. (2000).

This research made use of the cross-match service provided by CDS, Strasbourg.

This research has used data, tools, or materials developed as part of the EXPLORE project that has received funding from the European Union's Horizon 2020 research and innovation program under grant agreement No 101004214.

Facilities: CDS, MAST, IRTF (SpeX), VLT:Kueyen (X-Shooter), HST (NICMOS, STIS, WFC3/IR).

Software: Astropy (Astropy Collaboration et al. 2013, 2018), Astroquery (Ginsburg et al. 2017, 2019), Dust_extinction (Gordon et al. 2022), Dustmaps (Green 2018), Matplotlib (Hunter 2007), NumPy (van der Walt et al. 2011; Harris et al. 2020), Pandas (McKinney 2010, 2011), pwlf (Jekel & Venter 2007), PyVO (Graham et al. 2014), Seaborn (Waskom 2021), SciPy (Virtanen et al. 2020), Specutils (Earl et al. 2022), Stsynphot (STScI Development Team 2020), and Synphot (STScI Development Team 2018).

Appendix A
Machine-readable Tables

Table 4 lists all spectrum file names and their parent libraries, and the SIMBAD, 2MASS, and Gaia DR3 IDs of the target stars. Table 5 presents all synthetic 2MASS and HST magnitudes and uncertainties used in this work. Band-to-band covariance information is available upon request. Table 6 gives our adopted distance and reddening values. In-text previews are limited to 10 lines to demonstrate the table structure and

Table 4
Spectra and Star IDs

Spectrum	Library	SIMBAD	2MASS	Gaia DR3
109vir_stis_003	CALSPEC	* 109 Vir	14461493+0153344	3655377057091634304
10lac_stis_007	CALSPEC	* 10 Lac	22391567+3903011	1908095850396090880
16cygb_stis_003	CALSPEC	* 16 Cyg B	19415198+5031032	2135550755683407232
1732526_stisnic_007	CALSPEC	TYC 4424-1286-1	17325264+7104431	1651137131123978112
1740346_stisnic_005	CALSPEC	TYC 4207-219-1	17403468+6527148	1633143932573832448
1743045_stisnic_007	CALSPEC	2MASS J17430448+6655015	17430448+6655015	1634280312200704768
1757132_stiswfc_004	CALSPEC	TYC 4212-455-1	17571324+6703409	1633585107317144960
1802271_stiswfcnic_004	CALSPEC	BPS BS 17447-0067	18022716+6043356	2158745262705810304
1805292_stisnic_006	CALSPEC	TYC 4209-1396-1	18052927+6427520	2161093682102883712
1808347_stiswfc_004	CALSPEC	TYC 4433-1800-1	18083474+6927286	2260019315938461952

(This table is available in its entirety in machine-readable form.)

Table 5
Synthetic Magnitudes

	J		*H*		K_S		F110W		F125W		F160W	
Spectrum	mag	err	mag	err	mag	err	mag	err	mag	err	mag	err
109vir_stis_003	3.675	0.008	3.668	0.008	3.673	0.008	3.667	0.007	3.675	0.008	3.672	0.008
10lac_stis_007	5.273	0.013	5.388	0.009	5.486	0.007	5.212	0.015	5.273	0.013	5.356	0.010
16cygb_stis_003	5.017	0.008	4.676	0.008	4.635	0.008	5.140	0.007	5.012	0.008	4.732	0.008
1732526_stisnic_007	12.264	0.016	12.216	0.013	12.210	0.012	12.287	0.017	12.263	0.016	12.220	0.014
1740346_stisnic_005	12.059	0.016	11.977	0.013	11.967	0.012	12.101	0.016	12.059	0.016	11.990	0.014
1743045_stisnic_007	12.933	0.019	12.820	0.015	12.805	0.013	12.990	0.020	12.933	0.019	12.838	0.016
1757132_stiswfc_004	11.262	0.012	11.159	0.009	11.156	0.009	11.305	0.014	11.261	0.012	11.176	0.010
1802271_stiswfcnic_004	11.827	0.013	11.811	0.011	11.803	0.012	11.825	0.016	11.825	0.014	11.819	0.011
1805292_stisnic_006	12.017	0.016	11.973	0.013	11.972	0.012	12.037	0.017	12.017	0.016	11.978	0.014
1808347_stiswfc_004	11.623	0.014	11.539	0.011	11.550	0.009	11.665	0.016	11.622	0.014	11.554	0.011

(This table is available in its entirety in machine-readable form.)

Table 6
Adopted Distances and Reddenings

SIMBAD	Distance D (pc)	$\sigma_D^{\rm low}$ (pc)	$\sigma_D^{\rm high}$ (pc)	$E(B-V)$ (mag)	$\sigma_{E(B-V)}$ (mag)	D ref.	E ref.
* 109 Vir	41.1550	−0.3615	0.4828	0.0064	0.0004	1	13
* 10 Lac	454.9370	−32.5998	35.1707	0.0801	0.0036	1	13
* 16 Cyg B	21.1187	−0.0085	0.0081	0.0035	0.0003	1	13
TYC 4424-1286-1	1170.3805	−22.7738	24.0533	0.0196	0.0116	1	14
TYC 4207-219-1	1240.0450	−30.6903	28.6683	0.0287	0.0099	1	14
2MASS J17430448+6655015	1771.9917	−35.9045	37.0383	0.0363	0.0147	1	14
TYC 4212-455-1	1002.1997	−33.1524	38.7034	0.0508	0.0079	1	14
BPS BS 17447-0067	1514.9535	−52.2798	41.7642	0.0520	0.0102	1	14
TYC 4209-1396-1	1433.7218	−39.9004	33.1952	0.0316	0.0106	1	14
TYC 4433-1800-1	918.7812	−15.7393	13.4752	0.0415	0.0122	1	14

Note. References: (1) Bailer-Jones et al. (2021); (2) van Leeuwen (2007); (3) Bailer-Jones et al. (2018); (4) Maíz Apellániz et al. (2022); (5) Baumgardt & Vasiliev (2021); (6) Cantat-Gaudin & Anders (2020); (7) Schmidt et al. (2010); (8) Davies & Beasor (2020); (9) Torres et al. (2010); (10) Sahai et al. (2007); (11) Graczyk et al. (2020); (12) Pietrzyński et al. (2019); (13) Vergely et al. (2022); (14) Delchambre et al. (2023); (15) Skowron et al. (2021).

(This table is available in its entirety in machine-readable form.)

contents, and the full machine-readable tables are available in the online journal.

Appendix B
Comparison of Extinction Maps

We investigated a number of available line-of-sight extinction estimates for our sample of library stars, both from large-scale extinction maps and from parameter fits to individual stars. Of these, five are from 3D maps derived from aggregate spectrophotometric and parallax information (Chen et al. 2019; Green et al. 2019; Vergely et al. 2022; Lallement et al. 2022, 2018); three are from SED fitting techniques applied to individual library stars, including the values adopted for or derived from the original spectral library data (Anders et al. 2022; Andrae et al. 2023); and the remaining three are from 2D total line-of-sight maps (Schlafly & Finkbeiner 2011; Skowron et al. 2021; Delchambre et al. 2023).

A summary of all extinction data sources we considered is given in Table 7, including primary references, applied conversion factors from original data units to $E(B-V)$ if needed, and numbers of library stars for which extinction data are (a) available for a given star or distance-independent line of sight and (b) of those how many are considered valid measurements. For 3D maps we follow the `dustmaps` convention, where $E(B-V)$ values are considered valid for a given sightline within a specified range of distances. We consider single-star $E(B-V)$ measurements valid if they are free from data or fitting quality flags as defined by the respective references, if available.

Figure 15 shows pairwise comparisons for $E(B-V)$ values from the 3D maps and individual stellar fits, and the MAD of each of these is given in Table 8. The majority of the $E(B-V)$ measurements agree to within 0.05 or 0.1 mag, with the exception of GSP-Phot, which shows deviations of up to 0.25 mag.

Table 7
Summary of Extinction Data Sources

Kind	Name	$N^\star_{\rm total}$	$N^\star_{\rm valid}$	$E(B-V)$ conversion	Reference(s)	Comments
3D maps	G-TOMO v2	980	808	3.1^{-1}	Vergely et al. (2022)	
	G-TOMO v1	980	808	3.1^{-1}	Lallement et al. (2022)	
	StilISM	939	724	⋯	Lallement et al. (2018)	
	Bayestar19	891	238	0.884	Green et al. (2019)	
	Chen+19	480	377	0.75	Chen et al. (2019)	Gaia DR2 passbands
Single-star	StarHorse2021	619	425	3.3^{-1}	Anders et al. (2022)	
	GSP-Phot	533	533	3.1^{-1}	Andrae et al. (2023)	
	Library values	926	926	⋯	Rayner et al. (2009), Villaume et al. (2017), Verro et al. (2022b)	
2D maps	Gaia TGE	1020	1020	3.1^{-1}	Delchambre et al. (2023)	
	SFD	1061	1061	⋯	Schlafly & Finkbeiner (2011)	
	OGLE	76	76	0.808	Skowron et al. (2021)	Magellanic Clouds only

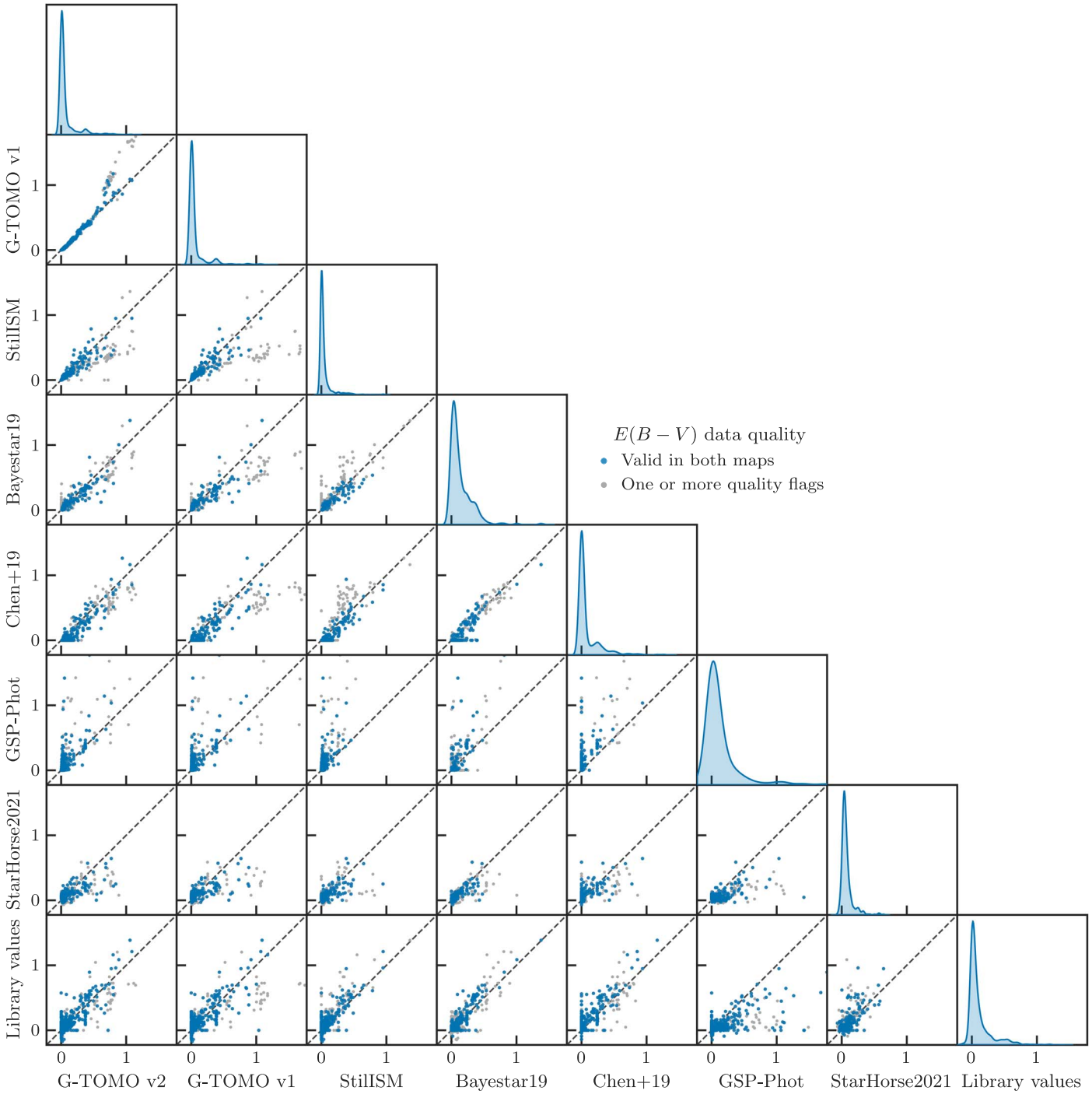

Figure 15. Pair plots of $E(B-V)$ measurements for stars common to the different extinction catalogs. Stars with high-quality measurements in both $E(B-V)$ maps per pair are shown by blue points, and stars with data quality flags in one or both maps are shown in light gray. Summary data for individual tables are given in Table 7, and the MADs of pairwise differences in Table 8.

Table 8
MADs of Pairwise $E(B-V)$ Differences for 3D Maps and Single-star Fits

	G-TOMO v2	G-TOMO v1	StilISM	Bayestar19	Chen+19	StarHorse2021	GSP-Phot	Library
G-TOMO v2	⋯	0.010	0.014	0.070	0.056	0.055	0.111	0.049
G-TOMO v1	0.010	⋯	0.016	0.086	0.066	0.058	0.110	0.050
StilISM	0.014	0.016	⋯	0.059	0.045	0.045	0.087	0.042
Bayestar19	0.070	0.086	0.059	⋯	0.053	0.050	0.243	0.072
Chen+19	0.056	0.066	0.045	0.053	⋯	0.064	0.250	0.076
StarHorse2021	0.055	0.058	0.045	0.050	0.064	⋯	0.105	0.056
GSP-Phot	0.111	0.110	0.087	0.243	0.250	0.105	⋯	0.169
Library	0.049	0.050	0.042	0.072	0.076	0.056	0.169	⋯

Notes. Please refer to Table 7 for descriptions of the extinction data sources.

ORCID iDs

M. J. Durbin https://orcid.org/0000-0001-7531-9815
R. L. Beaton https://orcid.org/0000-0002-1691-8217
A. J. Monson https://orcid.org/0000-0002-0048-2586
B. Swidler https://orcid.org/0000-0002-3749-4978
J. J. Dalcanton https://orcid.org/0000-0002-1264-2006

References

Allende Prieto, C. 2023, Atoms, 11, 61
Alvarez, R., Lancon, A., Plez, B., & Wood, P. R. 2000, A&A, 353, 322
Anders, F., Khalatyan, A., Queiroz, A. B. A., et al. 2022, A&A, 658, A91
Andrae, R., Fouesneau, M., Sordo, R., et al. 2023, A&A, 674, A27
Arentsen, A., Prugniel, P., Gonneau, A., et al. 2019, A&A, 627, A138
Aringer, B., Girardi, L., Nowotny, W., Marigo, P., & Bressan, A. 2016, MNRAS, 457, 3611
Aringer, B., Marigo, P., Nowotny, W., et al. 2019, IAUS, 343, 93
Astropy Collaboration, Price-Whelan, A. M., Sipőcz, B. M., et al. 2018, AJ, 156, 123
Astropy Collaboration, Robitaille, T. P., & Tollerud, E. J. 2013, A&A, 558, A33
Bagnulo, S., Jehin, E., Ledoux, C., et al. 2003, Msngr, 114, 10
Bailer-Jones, C. A. L., Rybizki, J., Fouesneau, M., Demleitner, M., & Andrae, R. 2021, AJ, 161, 147
Bailer-Jones, C. A. L., Rybizki, J., Fouesneau, M., Mantelet, G., & Andrae, R. 2018, AJ, 156, 58
Baldwin, C., McDermid, R. M., Kuntschner, H., Maraston, C., & Conroy, C. 2018, MNRAS, 473, 4698
Baumgardt, H., & Vasiliev, E. 2021, MNRAS, 505, 5957
Bell, C. P. M., Cioni, M. R. L., Wright, A. H., et al. 2019, MNRAS, 489, 3200
Bessell, M., & Murphy, S. 2012, PASP, 124, 140
Bohlin, R. C. 2007, in ASP Conf. Ser. 364, The Future of Photometric, Spectrophotometric and Polarimetric Standardization, ed. C. Sterken (San Francisco, CA: ASP), 315
Bohlin, R. C., & Cohen, M. 2008, AJ, 136, 1171
Bohlin, R. C., & Deustua, S. E. 2019, AJ, 157, 229
Bohlin, R. C., Deustua, S. E., & de Rosa, G. 2019, AJ, 158, 211
Bohlin, R. C., Dickinson, M. E., & Calzetti, D. 2001, AJ, 122, 2118
Bohlin, R. C., Gordon, K. D., & Tremblay, P. E. 2014, PASP, 126, 711
Bohlin, R. C., Mészáros, S., Fleming, S. W., et al. 2017, AJ, 153, 234
Bonatto, C., Bica, E., & Girardi, L. 2004, A&A, 415, 571
Calamida, A., Bajaj, V., Mack, J., et al. 2022, AJ, 164, 32
Cantat-Gaudin, T., & Anders, F. 2020, A&A, 633, A99
Carnall, A. C. 2017, arXiv:1705.05165
Casagrande, L., Ramírez, I., Meléndez, J., Bessell, M., & Asplund, M. 2010, A&A, 512, A54
Casagrande, L., & VandenBerg, D. A. 2018, MNRAS, 479, L102
Castelli, F., & Kurucz, R. L. 2003, in IAU Symp. 210, Modelling of Stellar Atmospheres, ed. N. Piskunov, W. W. Weiss, & D. F. Gray (San Francisco, CA: ASP), A20
Chen, B. Q., Guo, H. L., Gao, J., et al. 2022, MNRAS, 511, 1317
Chen, B. Q., Huang, Y., Yuan, H. B., et al. 2019, MNRAS, 483, 4277
Chen, Y. P., Trager, S. C., Peletier, R. F., et al. 2014, A&A, 565, A117
Choi, Y., Nidever, D. L., Olsen, K., et al. 2018, ApJ, 866, 90
Coelho, P. R. T., Bruzual, G., & Charlot, S. 2020, MNRAS, 491, 2025
Cohen, M., Wheaton, W. A., & Megeath, S. T. 2003, AJ, 126, 1090
Cushing, M. C., Vacca, W. D., & Rayner, J. T. 2004, PASP, 116, 362
Dahmer-Hahn, L. G., Riffel, R., Rodríguez-Ardila, A., et al. 2018, MNRAS, 476, 4459
Dalcanton, J. J., Williams, B. F., Melbourne, J. L., et al. 2012, ApJS, 198, 6
Davies, B., & Beasor, E. R. 2020, MNRAS, 493, 468
Delchambre, L., Bailer-Jones, C. A. L., Bellas-Velidis, I., et al. 2023, A&A, 674, A31
Earl, N., Tollerud, E., Jones, C., et al. 2022, astropy/specutils: V1.7.0, Zenodo, doi:10.5281/zenodo.6207491
Eftekhari, E., La Barbera, F., Vazdekis, A., Allende Prieto, C., & Knowles, A. T. 2022, MNRAS, 512, 378
Eriksson, K., Höfner, S., & Aringer, B. 2023, A&A, 673, A21
Fabricius, C., Luri, X., Arenou, F., et al. 2021, A&A, 649, A5
Falcón-Barroso, J., Sánchez-Blázquez, P., Vazdekis, A., et al. 2011, A&A, 532, A95
Fitzpatrick, E. L., Massa, D., Gordon, K. D., Bohlin, R., & Clayton, G. C. 2019, ApJ, 886, 108
Gaia Collaboration, Montegriffo, P., & Bellazzini, M. 2023, A&A, 674, A33
Ginsburg, A., Parikh, M., Woillez, J., et al., 2017 Astroquery: Access to Online data Resources, Astrophysics Source Code Library, ascl:1708.004
Ginsburg, A., Sipőcz, B. M., Brasseur, C. E., et al. 2019, AJ, 157, 98
Girardi, L., Dalcanton, J., Williams, B., et al. 2008, PASP, 120, 583
Gonneau, A., Lancon, A., Trager, S. C., et al. 2016, A&A, 589, A36
Gonneau, A., Lancon, A., Trager, S. C., et al. 2017, A&A, 601, A141
Gonneau, A., Lyubenova, M., Lancon, A., et al. 2020, A&A, 634, A133
Gordon, K., Larson, K., McBride, A., et al. 2022, dust_extinction, v1.1, GitHub, https://github.com/karllark/dust_extinction/releases/tag/v1.1
Gordon, K. D., Clayton, G. C., Misselt, K. A., Landolt, A. U., & Wolff, M. J. 2003, ApJ, 594, 279
Graczyk, D., Pietrzyński, G., Thompson, I. B., et al. 2020, ApJ, 904, 13
Graham, M., Plante, R., Tody, D., & Fitzpatrick, M., 2014 PyVO: Python access to the Virtual Observatory, Astrophysics Source Code Library, ascl:1402.004
Green, G. 2018, JOSS, 3, 695
Green, G. M., Schlafly, E., Zucker, C., Speagle, J. S., & Finkbeiner, D. 2019, ApJ, 887, 93
Gregg, M. D., Silva, D., Rayner, J., et al. 2006, in The 2005 HST Calibration Workshop: Hubble After the Transition to Two-Gyro Mode, ed. A. M. Koekemoer, P. Goudfrooij, & L. L. Dressel, Vol. 209 (Baltimore, MD: STScI), 209
Harris, C. R., Millman, K. J., van der Walt, S. J., et al. 2020, Natur, 585, 357
Hartig, G. F. 2009, WFC3 SMOV Programs 11437/9: IR On-orbit PSF Evaluation, Space Telescope WFC Instrument Science Report
Haschke, R., Grebel, E. K., & Duffau, S. 2011, AJ, 141, 158
Holberg, J. B., & Bergeron, P. 2006, AJ, 132, 1221
Hunter, J. D. 2007, CSE, 9, 90
Imara, N., & Blitz, L. 2007, ApJ, 662, 969
Jekel, C. F., & Venter, G. 2019, pwlf: A Python Library for Fitting 1D Continuous Piecewise Linear Functions, https://github.com/cjekel/piecewise_linear_fit_py
John, T. L. 1988, A&A, 193, 189
Joshi, Y. C., & Panchal, A. 2019, A&A, 628, A51
Koornneef, J., Bohlin, R., Buser, R., Horne, K., & Turnshek, D. 1986, HiA, 7, 833
Lallement, R., Babusiaux, C., Vergely, J. L., et al. 2019, A&A, 625, A135
Lallement, R., Capitanio, L., Ruiz-Dern, L., et al. 2018, A&A, 616, A132
Lallement, R., Vergely, J. L., Babusiaux, C., & Cox, N. L. J. 2022, A&A, 661, A147

Lancon, A., Gonneau, A., Trager, S. C., et al. 2019, in IAU Symp. 343, Why Galaxies Care About AGB Stars: A Continuing Challenge through Cosmic Time (Cambridge: Cambridge Univ. Press), 309
Lancon, A., Gonneau, A., Verro, K., et al. 2021, A&A, 649, A97
Le Borgne, J. F., Bruzual, G., Pelló, R., et al. 2003, A&A, 402, 433
Levesque, E. M., Massey, P., Olsen, K. A. G., et al. 2006, ApJ, 645, 1102
Lyubenova, M., Kuntschner, H., Rejkuba, M., et al. 2012, A&A, 543, A75
Maíz Apellániz, J., Barbá, R. H., Fernández Aranda, R., et al. 2022, A&A, 657, A131
Maíz Apellániz, J., & Pantaleoni González, M. 2018, A&A, 616, L7
Maíz Apellániz, J., & Weiler, M. 2018, A&A, 619, A180
Maraston, C. 2005, MNRAS, 362, 799
McKinney, W. 2010, in Proc. 9th Python in Science Conf., ed. S. van der Walt & J. Millman (Austin, TX: SciPy), 56
McKinney, W. 2011, Python for High Performance and Scientific Computing
Ochsenbein, F., Bauer, P., & Marcout, J. 2000, A&AS, 143, 23
Pietrzyński, G., Graczyk, D., Gallenne, A., et al. 2019, Natur, 567, 200
Prugniel, P., & Soubiran, C. 2001, A&A, 369, 1048
Prugniel, P., & Soubiran, C. 2004, arXiv:astro-ph/0409214
Prugniel, P., Soubiran, C., Koleva, M., & Le Borgne, D. 2007, arXiv:astro-ph/0703658
Rayner, J. T., Cushing, M. C., & Vacca, W. D. 2009, ApJS, 185, 289
Rayner, J. T., Toomey, D. W., Onaka, P. M., et al. 2003, PASP, 115, 362
Riess, A. G. 2011, An Independent Determination of WFC3-IR Zeropoints and Count Rate Non-Linearity from 2MASS Asterisms, Space Telescope WFC Instrument Science Report
Ripepi, V., Chemin, L., Molinaro, R., et al. 2022, MNRAS, 512, 563
Ripepi, V., Cioni, M. R. L., Moretti, M. I., et al. 2017, MNRAS, 472, 808
Sahai, R., Morris, M., Sánchez Contreras, C., & Claussen, M. 2007, AJ, 134, 2200
Sánchez-Blázquez, P., Peletier, R. F., Jiménez-Vicente, J., et al. 2006, MNRAS, 371, 703
Schlafly, E. F., & Finkbeiner, D. P. 2011, ApJ, 737, 103
Schmidt, S. J., West, A. A., Hawley, S. L., & Pineda, J. S. 2010, AJ, 139, 1808
Scolnic, D. M., Jones, D. O., Rest, A., et al. 2018, ApJ, 859, 101
Skowron, D. M., Skowron, J., Udalski, A., et al. 2021, ApJS, 252, 23
Skrutskie, M. F., Cutri, R. M., Stiening, R., et al. 2006, AJ, 131, 1163
Straizys, V. 1998, BaltA, 7, 571
Strömgren, B. 1937, Aufgaben und Probleme der Astrophotometrie, 26 (Leipzig: Akademische verlagsgesellschaft M.B.H.), 319
STScI Development Team, 2018 synphot: Synthetic photometry using Astropy, Astrophysics Source Code Library, ascl:1811.001
STScI Development Team., 2020 stsynphot: synphot for HST and JWST, Astrophysics Source Code Library, ascl:2010.003
Taylor, B. J. 1986, ApJS, 60, 577
Tej, A., Lancon, A., Scholz, M., & Wood, P. R. 2003, A&A, 412, 481
Tonry, J. L., Stubbs, C. W., Lykke, K. R., et al. 2012, ApJ, 750, 99
Torres, G., Andersen, J., & Giménez, A. 2010, A&ARv, 18, 67
Trager, S. C. 2012, in ASI Conf. Ser. 6, International Workshop on Stellar Libraries, ed. P. Prugniel & H. P. Singh (Hyderabad: ASI), 1
Turnshek, D. A., Bohlin, R. C., Williamson, R. L., et al. 1990, AJ, 99, 1243
Vacca, W. D., Cushing, M. C., & Rayner, J. T. 2003, PASP, 115, 389
Vacca, W. D., Cushing, M. C., & Rayner, J. T. 2004, PASP, 116, 352
Valdes, F., Gupta, R., Rose, J. A., Singh, H. P., & Bell, D. J. 2004, ApJS, 152, 251
van der Walt, S., Colbert, S. C., & Varoquaux, G. 2011, CSE, 13, 22
van Leeuwen, F. 2007, A&A, 474, 653
Vergely, J. L., Lallement, R., & Cox, N. L. J. 2022, A&A, 664, A174
Verro, K., Trager, S. C., Peletier, R. F., et al. 2022a, A&A, 661, A50
Verro, K., Trager, S. C., Peletier, R. F., et al. 2022b, A&A, 660, A34
Villaume, A., Conroy, C., Johnson, B., et al. 2017, ApJS, 230, 23
Virtanen, P., Gommers, R., Oliphant, T. E., et al. 2020, NatMe, 17, 261
Wang, C., Liu, X. W., Huang, Y., et al. 2018, MNRAS, 480, 4766
Waskom, M. 2021, JOSS, 6, 3021
Wenger, M., Ochsenbein, F., Egret, D., et al. 2000, A&AS, 143, 9
Yan, R., Chen, Y., Lazarz, D., et al. 2019, ApJ, 883, 175
Yuan, H. B., Liu, X. W., & Xiang, M. S. 2013, MNRAS, 430, 2188